

# Synergistic effect of the electronic band delocalization and bond anharmonicity on the thermoelectric performance of $\text{Cs}_2\text{TeX}_6$ (X=Cl, Br, I)

Heena<sup>†1</sup>, Vineet Kumar Pandey<sup>†2</sup>, Saanvi Marethiya<sup>3</sup>, Ambesh Dixit<sup>4</sup>, Ajay Singh Verma<sup>\*5</sup>,  
and K.C. Bhamu<sup>\*3</sup>

<sup>1</sup>Department of Physics, Jamia Millia Islamia, New Delhi 110025, India

<sup>2</sup>Department of Physics, Govt Naveen College Janakpur, M.C.B. 497778, Chhattisgarh,  
India

<sup>3</sup>Department of Physics, SLAS, Mody University of Science and Technology,  
Lakshmangarh, Sikar, Rajasthan, 332311, India

<sup>4</sup>Advanced Materials and Device Laboratory, Department of Physics, Indian Institute of  
Technology, Jodhpur 342037, India

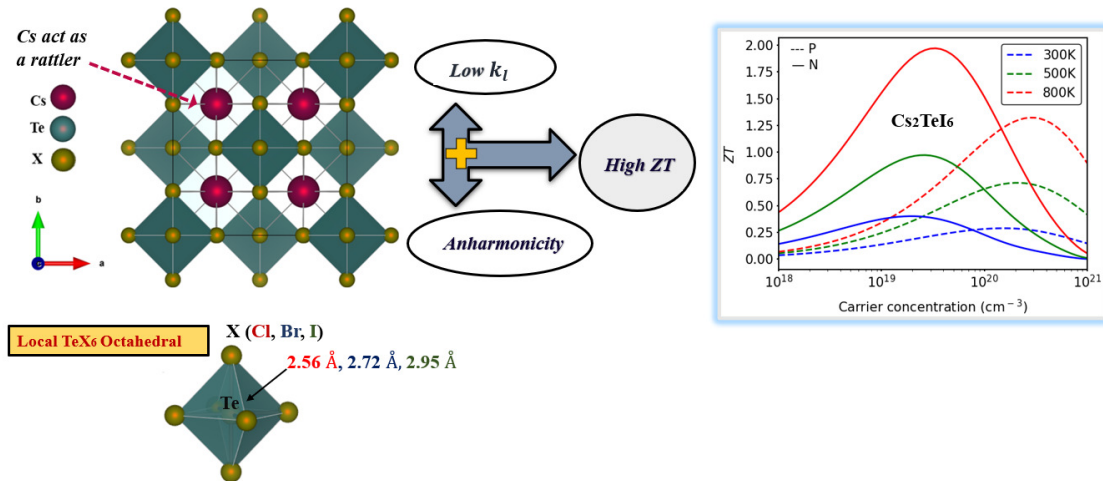
<sup>5</sup>Department of Physics, Anand School of Engineering and Technology, Sharda University  
Agra, Keetham, Agra, 282007

February 3, 2026

---

<sup>†</sup>These authors contributed equally to this work

<sup>\*</sup>Corresponding author. Email: kcbhamu85@gmail.com



**keywords**

- Vacancy ordered double halide perovskites
- Ultralow lattice thermal conductivity
- Inverse participation ratio
- High power factor and ZT

# 1 Abstract

We investigate the structural, mechanical, and the thermoelectric properties of lead-free double halide perovskites  $\text{Cs}_2\text{TeX}_6$  ( $\text{X}=\text{Cl}, \text{Br}, \text{I}$ ) by employing first-principles calculations and semiclassical Boltzmann transport theory. The HSE06 band gap is incorporated using scissor correction method along with PBE calculated electronic band structure including spin-orbit coupling (SOC) to accurately predict the transport properties. The band gap values are 3.27, 2.50 and 1.55 eV for  $\text{Cs}_2\text{TeX}_6$  ( $\text{X}=\text{Cl}, \text{Br}, \text{I}$ ) respectively. The coexistence of heavy and light bands in the case of  $\text{Cs}_2\text{TeI}_6$  band structure helps to mitigate trade-off between the Seebeck coefficient ( $S$ ) and electrical conductivity ( $\sigma$ ). Among these systems,  $\text{Cs}_2\text{TeI}_6$  exhibits superior performance with a remarkable ZT of 1.97 at 800 K and electronic concentration  $3.35 \times 10^{19} \text{ cm}^{-3}$ . Such a high ZT at significantly low carrier concentration is the result of high electrical conductivity along with low lattice thermal conductivity. The lattice thermal conductivity ( $\kappa_l$ ) of  $\text{Cs}_2\text{TeI}_6$  was found to be  $0.41 \text{ W m}^{-1} \text{ K}^{-1}$  at room temperature. Such a low  $\kappa_l$  is attributed to the presence of weak Te-I bond and non-uniform out-of-phase displacement of Cs atoms. The presence of local octahedra  $\text{TeX}_6$  along with weak bonds offers strong resistance to heat conduction and, in turn, lattice thermal conductivity is suppressed drastically. In particular, transverse acoustic phonons along with optical phonons significantly limit the lattice thermal conductivity. Taken together, these results position  $\text{Cs}_2\text{TeI}_6$  as a strong candidate for high performance thermoelectric applications.

## 2 Introduction

The rapid requirement in global energy consumption is driving fossil fuel exhaustion at a very high pace and causing severe damage to the environment and global warming. In response, scientists are more focused on adopting renewable energy resources and efficient use of energy to avoid energy losses. One promising way out is the reuse of waste heat generated by primary energy resources. Thermoelectrics have emerged as a clean source of electrical energy by utilizing heat as an input [1–4]. Thermoelectric materials promise many advantages such as no waste output, no moving parts involved and it alleviates further pollution increase by reusing the waste energy [2]. Conventionally, a thermoelectric material's conversion efficiency is defined by figure of merit ( $ZT$ ) =  $\frac{S^2 \sigma T}{\kappa_e + \kappa_l}$ , in which  $S$ ,  $\kappa_e$ ,  $\kappa_l$ ,  $\sigma$  and  $T$  are the Seebeck coefficient, electronic thermal conductivity, lattice thermal conductivity, electrical conductivity and absolute temperature, respectively [5, 6]. In principle, high Seebeck coefficient, low thermal conductivity and high electrical conductivity ( $\kappa = \kappa_e + \kappa_l$ ) need to be possessed by a material in order to be highly efficient in energy conversion. Since there is a tradeoff between  $S$  and  $\sigma$  on the scattering mechanism and carrier concentration, they cannot be increased simultaneously, i.e., the increase in  $S$  is followed by decrease in  $\sigma$  and vice versa. Apart from this, another approach to make these materials energy efficient is by hindering the phonon transport using defects, scattering or doping [7–10]. The latter approach of reducing phonon transport is easier as compared to enhancing electrical conductivity and the Seebeck coefficient. There is another route to look for a new class of materials that inherently accommodates high atomic weight, disorder introduced using dopants, the rattling motion or the polyhedra within the unit cell that enhance the phonon scattering and have intrinsic low lattice thermal conductivity thereby improving the efficiency of thermoelectric materials.

The perovskite family offers many opportunities to overcome challenges posed to thermoelectric performance by making use of its immense structural and diverse compositions [11–17]. These perovskites adopt the cubic structure with the chemical formula  $\text{ABX}_3$ , where A and B are positively charged cations, atom X is a halogen atom, and atom A is larger than B in size [18]. Here atoms A and B are surrounded by anions in cuboctahedral and octahedral coordination, respectively. Later it was found that the size of A, B and X atoms significantly affects the stability and has high defect density [19–21]. There are not many options available to tune the band gap of these perovskites [22]. To overcome these, scientists introduced two cations to enable better size matching. Such structures have better stability, flexibility and better control over band gap tunability and are called double perovskite with chemical formula  $\text{A}_2\text{BB}'\text{X}_6$ . Double perovskites are a very versatile class of material including organic, inorganic or hybrid [12, 23–28]. Scientists have extensively exploited these materials for their optical, photochemical, transport, and various other prop-

erties [24–27, 29–33]. In addition to being environmentally friendly and innocuous, these materials offer strong mechanical and dynamical stability, are easily synthesized, etc [34–36]. These materials have been harnessed in light-emitting diode, solar cells and laser applications for their interesting properties [37–41]. In particular, lead halide perovskites have been reported to have low lattice thermal conductivity due to their unique lattice dynamics such as  $\text{CsPbI}_3$ ,  $\text{CsPbBr}_3$ ,  $\text{CsSnI}_3$  [42]. Although these systems provided very promising solution for thermoelectric applications, it was discarded for lead being toxic and Sn being unstable in the air at ambient conditions. Further, these perovskites do not exhibit better electrical transport properties as these have high band gaps (typically  $\geq 1.8$  eV) that restrict the electron conduction and pose a significant challenge [43]. Hence it is crucial to discover new material with better electrical properties and lower thermal conductivity. Lately, a distortion was introduced in the form of vacancy in double halide perovskite at the B site to make vacancy ordered double perovskite with chemical formula  $\text{A}_2\text{BX}_6$  [44–46]. The creation of the vacancy further improved the stability. Studies have suggested that accommodation of distortion in the local structure acts as a scattering point and significantly lowers the lattice thermal conductivity [47–49]. The obvious distinction between the structure of perovskites  $\text{A}_2\text{BB}'\text{X}_6$  and  $\text{A}_2\text{BX}_6$  is the local surrounding of the octahedra in  $\text{A}_2\text{BX}_6$ . The  $\text{BX}_6$  octahedra share the corner in the former case, while it remains isolated in the latter case.

Recently, a vacancy ordered double perovskite  $\text{Cs}_2\text{TeI}_6$  has garnered significant attention due to its photovoltaic, optoelectronic properties, excellent absorption coefficient, stable X-ray detectors, energy storage applications and photodetector [50–53].  $\text{Cs}_2\text{TeI}_6$  has been experimentally synthesized [50, 54, 55]. Interestingly, the defect tolerance limit of this system  $\text{Cs}_2\text{TeI}_6$  is significantly lower [56]. The band gap of this system is in the visible range (1.5–1.8 eV) [56]. In addition to this, Siad et al., showed the thermoelectric performance of  $\text{Cs}_2\text{TeBr}_6$  and  $\text{Cs}_2\text{TeI}_6$  at GGA-PBE level [57]. This study did not thoroughly analysed the transport properties. Lately, Zheng et al predicted that  $\text{Cs}_2\text{TeI}_6$  has ultralow lattice thermal conductivity [58]. In this work, we present the systematic study of structural, electronic, mechanical, vibrational and thermoelectric properties of  $\text{Cs}_2\text{TeX}_6$  ( $\text{X}=\text{Cl, Br, I}$ ).

### 3 Computational methodology

Our first-principles calculations were based on the density functional theory as implemented in the Vienna Ab Initio Simulation Package (VASP) with the projector augmented wave (PAW) method [59–61]. The exchange correlation potential of electrons was described by the Perdew-Burke-Ernzerhof (PBE) generalized gradient approximation (GGA) while optimizing the structure [62]. As PBE underestimates band gap and to account for the fundamental self interaction error in PBE functional, we used Heyd-Scuseria-Ernzerhof (HSE06) method with an automatic  $\Gamma$ -centered k-mesh with resolution  $0.025 \text{ \AA}^{-1}$  and 63 irreducible k-points for better prediction of band gaps and electronic properties [63]. We used an energy cutoff of 500 eV to truncate the plane wave basis used in Kohn-Sham wave functions. We optimized the structure until the Hellmann-Feynman force on each atom was less than  $0.01 \text{ eV\AA}^{-1}$ . We investigated the bonding analysis using the LOBSTER package [64]. We computed the phonon dispersion using PHONOPY to confirm the dynamical stability of these systems [65]. We used a q-mesh  $5 \times 5 \times 5$  for phonon calculations. We computed the transport properties by solving the Boltzmann transport equation as implemented in AMSET code [66]. We plotted the electronic band structure and transport properties using SUMO code [67]. The structure and displacement modes were visualized using VESTA code [68]. In order to calculate the lattice thermal conductivity, we used the Debye-Callaway model as incorporated in the AICON code [69]. The input parameters needed to do this calculation such as phonon frequencies, group velocity and Grüneisen parameter were computed using PHONOPY [65]. We calculated the Grüneisen parameter using phonon calculation of optimized structure and 0.4% up and down in volume.

## 4 Results and Discussion

### 4.1 Crystal structure optimization

$\text{Cs}_2\text{TeX}_6$  ( $\text{X}=\text{Cl}, \text{Br}, \text{I}$ ) are vacancy-ordered double halide perovskites that crystallize in a face-centered cubic (FCC) crystal structure with space group  $Fm\bar{3}m$  [57, 70]. The crystallographic representation of the unit cell is illustrated in Fig. 1(a) and (b). In this configuration, a unit cell of  $\text{Cs}_2\text{TeX}_6$  accommodates  $[\text{TeX}_6]^{-2}$  octahedra along with a cation  $\text{Cs}^{+1}$  present in the void between the octahedra. These  $[\text{TeX}_6]^{-2}$  octahedra do not share edges, faces or corners. The  $\text{TeX}_6$  octahedra establish 12-fold coordination environment of  $\text{X}$  anions.  $\text{Cs}$ ,  $\text{Te}$ , and  $\text{X}$  atoms are situated at 8c Wyckoff site with  $(0.25, 0.25, 0.25)$ , 4a Wyckoff site with  $(0, 0, 0)$ , and  $\text{X}$  anions at 24e Wyckoff site  $(0.2498, 0, 0)$  fractional coordinates, respectively. The  $\text{Cs}$  atom is embedded within the framework of  $\text{TeX}_6$  octahedra. We have simulated the crystal geometry using GGA-PBE. Our calculations reveal that the  $\text{Te}-\text{Cl}$ ,  $\text{Te}-\text{Br}$  and  $\text{Te}-\text{I}$  bonds are around  $2.56 \text{ \AA}$ ,  $2.73 \text{ \AA}$ , and  $2.95 \text{ \AA}$ , respectively. The increasing bond length is attributed to decreasing electronegativity. The calculated lattice parameter of these systems  $\text{Cs}_2\text{TeX}_6$  ( $\text{X}=\text{Cl}, \text{Br}, \text{I}$ ) were found to be  $10.51 \text{ \AA}$ ,  $10.97 \text{ \AA}$ , and  $11.69 \text{ \AA}$ , respectively. The increasing trend of lattice parameters is attributed to the increasing atomic radius of halides. These obtained values are in good agreement with the experimental and computational reports [56, 70]. Due to the increasing volume of unit cell with increasing halides atomic number, the  $\text{Cs}-\text{X}$  bond length is found to increase to be  $3.72 \text{ \AA}$ ,  $3.88 \text{ \AA}$ , and  $4.13 \text{ \AA}$ , for  $\text{Cl}$ ,  $\text{Br}$  and  $\text{I}$ , respectively. In other words, the void space between the  $\text{TeX}_6$  octahedra is increasing. The other structural details for  $\text{Cs}_2\text{TeX}_6$  ( $\text{X}=\text{Cl}, \text{Br}, \text{I}$ ) are provided in the table S1 of supplementary information.

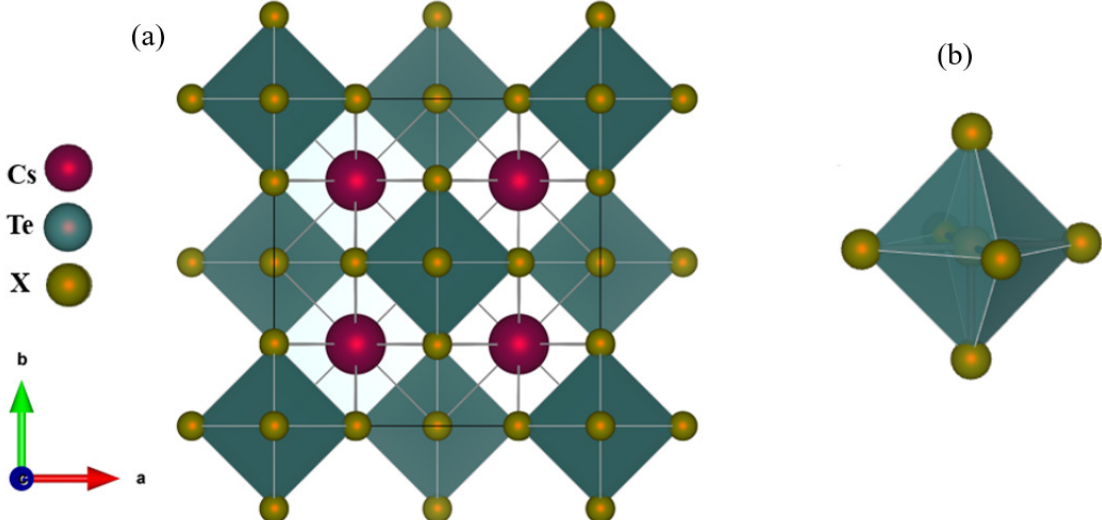


Figure 1: Crystal structure of vacancy ordered double halide perovskite (a)  $\text{Cs}_2\text{TeX}_6$  ( $\text{X} = \text{Cl}, \text{Br}, \text{I}$ ), (b) Octahedra structure ( $\text{TeX}_6$ )

### 4.2 Bonding analysis

Figures 2(a), (b) and (c) display the projected crystal orbital Hamilton population (pCOHP) curves for the respective  $\text{X}-\text{Te}$  bonds in  $\text{Cs}_2\text{TeX}_6$  ( $\text{X}=\text{Cl}, \text{Br}, \text{I}$ ). The  $-\text{pCOHP}$  peak for other bonds is included in supporting information. The negative values on the  $\text{X}$ -axis represent antibonding states, with those below the Fermi energy indicating instability in the system. Our analysis of the  $-\text{pCOHP}$  curve reveals that with decrease in the electronegativity of the  $\text{X}$  atom, the heights of the  $-\text{pCOHP}$  peak decreases. However, we do not notice any significant shift of these peaks on the energy axis. This shortening of peaks is attributed to

the diffused Iodine  $p$  orbitals as compared to the Chlorine and Bromine  $p$  orbitals. The decreasing heights of the peak imply reduction in orbital overlap, for instance, the I-Te has the least orbital overlap and the Cl-Te has the most orbital overlap. Orbital overlapping is related to the strength of bonds. In our case, I-Te bond is weaker than the Cl-Te and the Br-Te bond. Further, weak bonds generally correspond to more anharmonicity. Increased anharmonicity negatively impacts the lattice thermal conductivity and reduces it further [71]. These primary results motivate to investigate further its thermoelectric properties.

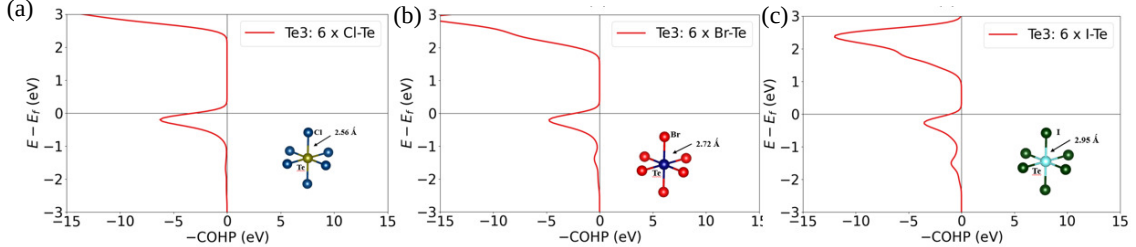


Figure 2: Projected crystal orbital Hamilton population of vacancy ordered perovskite derivatives for Cl-Te bond in (a)  $\text{Cs}_2\text{TeCl}_6$  (b)  $\text{Cs}_2\text{TeBr}_6$  (c)  $\text{Cs}_2\text{TeI}_6$

### 4.3 Electronic properties

Figure 3 depicts the electronic band structure along with the partial density of states (DOS) of  $\text{Cs}_2\text{TeX}_6$  ( $\text{X}=\text{Cl, Br, and I}$ ) using HSE06 hybrid functional including spin-orbit coupling. These materials are found to be semiconductors with electronic band gap values of 3.27 eV, 2.50 eV, and 1.55 eV, respectively at the HSE06 level. The decrease in band gap values is attributed to the decreasing electronegativities of Cl, Br, and I, and in turn increasing bond length of Te-Cl, Te-Br, and Te-I, respectively. Table 1 contains all calculated band gaps with different functionals along with respective experimental values from the reported literature. This matches well with the reported bandgaps in the available reports [50, 56, 72, 73]. The valence band maxima (VBM) and conduction band minima (CBM) of  $\text{Cs}_2\text{TeCl}_6$  and  $\text{Cs}_2\text{TeBr}_6$  lie at W and L high symmetry points of the Brillouin zone, respectively. However, the VBM of  $\text{Cs}_2\text{TeI}_6$  shifts to  $\Gamma$  point and CBM remains intact at L point. We do not notice any prominent change in the conduction band dispersion in  $\text{Cs}_2\text{TeX}_6$  ( $\text{X}=\text{Cl, Br, I}$ ), whereas there is significant improvement in the valence band dispersion. This modification in the band structure is present in DOS as well. Apart from this, the VBM is doubly degenerate in all the system  $\text{Cs}_2\text{TeX}_6$  ( $\text{X}=\text{Cl, Br, I}$ ). However, CBM is doubly degenerate in  $\text{Cs}_2\text{TeCl}_6$  and  $\text{Cs}_2\text{TeBr}_6$  and quadruply degenerate in  $\text{Cs}_2\text{TeI}_6$ . This higher degeneracy in CBM gives  $\text{Cs}_2\text{TeI}_6$  an edge over the other two systems  $\text{Cs}_2\text{TeCl}_6$  and  $\text{Cs}_2\text{TeBr}_6$  from thermoelectric perspective. Table 2 shows the effective mass of these systems along different directions of the Brillouin zone. Notably, there is presence of heavy holes and light holes together at the VBM for  $\text{Cs}_2\text{TeCl}_6$  and  $\text{Cs}_2\text{TeBr}_6$ , while such feature in VBM of  $\text{Cs}_2\text{TeI}_6$  is absent. The partial DOS analysis reveals that Te- $p$  and X- $p$  states have predominantly contributed to the valence band along with the minor contribution of Te- $s$  states near VBM, while in the conduction band, Te- $p$  states have dominant contribution. The significant dispersion of the conduction and valence band is attributed to the delocalized nature of  $p$  orbitals. These combinations of different types of carriers have previously been reported to enhance the thermoelectric performance [74, 75].

Table 1: Calculated electronic Band gaps of  $\text{Cs}_2\text{TeX}_6$  ( $\text{X} = \text{Cl, Br, I}$ ) using different functionals

VODPs	Calculated band gap (eV)			Reported band gap (eV)	
	PBE	HSE06	HSE06+SOC	Theory	Experimental
$\text{Cs}_2\text{TeCl}_6$	2.66	3.53	3.27	3.4	3.15 [73]
$\text{Cs}_2\text{TeBr}_6$	1.97	2.72	2.50	2.7	2.68 [73]
$\text{Cs}_2\text{TeI}_6$	1.18	1.85	1.55	1.83	1.59 [50, 56]

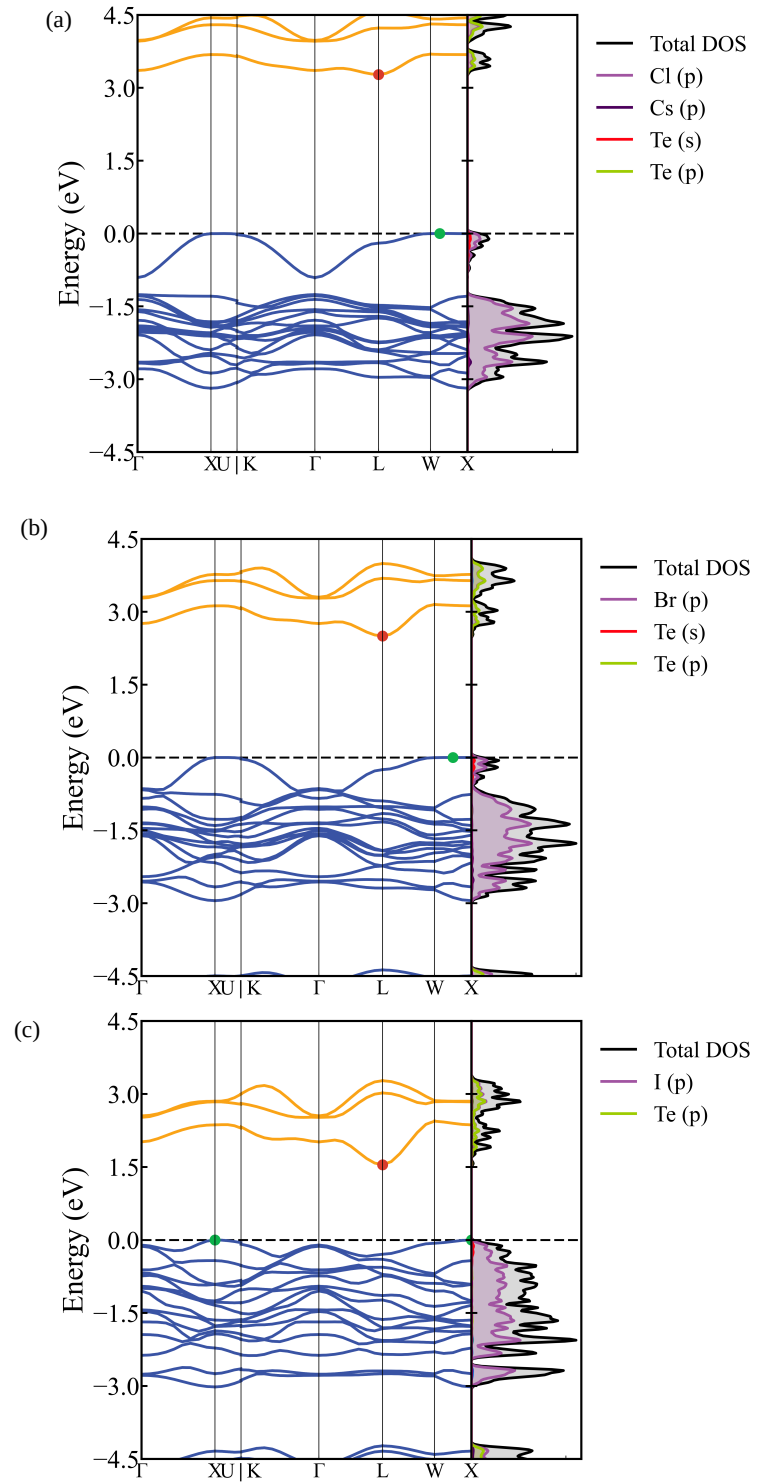


Figure 3: Electronic band structure along with DOS of (a)  $\text{Cs}_2\text{TeCl}_6$  , (b)  $\text{Cs}_2\text{TeBr}_6$ , and (c)  $\text{Cs}_2\text{TeI}_6$ .

#### 4.4 Vibrational properties and electron localization function (ELF)

Figures 4 (a), (b), and (c) present the phonon band dispersion along the high-symmetry points of the Brillouin zones, along with the phonon partial density of states (PDOS) for  $\text{Cs}_2\text{TeCl}_6$ ,  $\text{Cs}_2\text{TeBr}_6$ , and  $\text{Cs}_2\text{TeI}_6$

respectively. We notice the presence of small imaginary frequency near the *Gamma* point in  $\text{Cs}_2\text{TeI}_6$ . However,  $\text{Cs}_2\text{TeCl}_6$  and  $\text{Cs}_2\text{TeBr}_6$  had no imaginary frequency. Such small imaginary frequencies are insignificant and can be overcome with larger supercells [76]. Hence, all these systems are dynamically stable. We notice the presence of a small imaginary frequency near  $\Gamma$  point for  $\text{Cs}_2\text{TeI}_6$ . Such small imaginary frequencies are the results of computational inaccuracy. Going down in the halogen group from Cl to I, the unit cell accommodates more atomic mass and in turn, the vibrational frequencies soften. This softening leads to lower phonon energy and diminished Debye temperature thereby helping in reducing lattice thermal conductivity. For instance, the Debye temperature for  $\text{Cs}_2\text{TeCl}_6$ ,  $\text{Cs}_2\text{TeBr}_6$ , and  $\text{Cs}_2\text{TeI}_6$ , estimated from their phonon band dispersion, are 412 K, 309 K, and 254 K, respectively. The atom projected phonon DOS reveals that the Cs atoms have a dominant contribution near the low frequency range. In the mid frequency range, the halogen atom has significant contribution with minor contribution from Te atoms. However, Te has mostly contributed near the high frequency range. Our comparison of phonon DOS reveals that the phonon DOS increases as we go from Cl to I, particularly at low range frequencies. Increasing the phonon DOS has previously been reported to cause higher phonon scattering and lower lattice thermal conductivity as low energy phonons are primarily responsible for heat transport. Additionally, in order to have an insightful trend of the nature of chemical bonding and electron distribution that directly affects the lattice dynamics and phonon scattering, we plotted the electron localization function. Figure 4(d), (e), and (f) show ELF plot of (110) plane of  $\text{Cs}_2\text{TeCl}_6$ ,  $\text{Cs}_2\text{TeBr}_6$ , and  $\text{Cs}_2\text{TeI}_6$ , respectively. In these figures 4(d), (e) and (f), the red green and blue zone in the ELF isosurfaces around the Te-X bond exhibits the high electron localization, free electron-like feature, and low electron density region, respectively. The comparative analysis of these ELF reveals that the ELF isosurface appears sharply localized as the red lobe is compact and tightly confined in  $\text{Cs}_2\text{TeCl}_6$ , suggesting directional covalent interaction. The localized nature of the Te-Cl bond indicates its harmonic nature. Such feature of Te-Cl makes this system have lower phonon scattering and high lattice thermal conductivity. Transitioning to  $\text{Cs}_2\text{TeBr}_6$ , we notice a subtle increase in spatial extent and diffusivities in the ELF isosurface of the Te-Br bond as the red lobe is now slightly more diffused. These diffusivities around the ELF isosurface of the Te-Br bond reflect the softening of the bond and increasing bond weakness and anharmonicity as compared to the Te-Cl bond. Such features help in greater atomic displacement and enhanced phonon-phonon interactions. This diffused nature of the red lobes in ELF isosurface of  $\text{Cs}_2\text{TeI}_6$  becomes more prominent for the Te-I bond. The bonding region in the Te-I are more delocalized and widely spread, indicating a comparatively weak and anharmonic bond. This pronounced anharmonicity is a key contributor to phonon-phonon scattering, leading to a substantial reduction in the lattice thermal conductivity. Overall, our comparative analysis reveals that going from Cl to I as the electronegativity decreases, the electron localization decreases, and bond anharmonicity increases causing suppression of lattice thermal conductivity. These results are indicative of a better thermoelectric performance in  $\text{Cs}_2\text{TeX}_6$  (X=Cl, Br, I). Apart from this, we have performed the ab initio molecular dynamics (AIMD) simulations in the NVT ensemble using the Nose-Hoover thermostat at 300 K, as shown in Figure S6 for  $\text{Cs}_2\text{TeBr}_6$  and S7 for  $\text{Cs}_2\text{TeI}_6$ , the crystal framework remains intact over the long timescale of 10 ps. Throughout the simulation time, no significant structural distortion and bond breaking is observed, confirming its dynamical stability. The persistence of equilibrium over long simulation time scale indicates that these systems can maintain its integrity at 300 K.

Table 2: Carrier effective masses along different directions of the Brillouin zone

System	$m_h^*/m_e$				$m_e^*/m_e$			
	W-X ( $\Gamma$ - X)	W-K ( $\Gamma$ - K)	W-U ( $\Gamma$ - L)	W-L	L- $\Gamma$	L-U	L-W	L-K
$\text{Cs}_2\text{TeCl}_6$	10.442	2.986	2.986	1.577	1.446	0.643	0.643	0.643
$\text{Cs}_2\text{TeBr}_6$	15.491	2.624	2.624	1.302	0.702	0.380	0.380	0.380
$\text{Cs}_2\text{TeI}_6$	(0.607, 0.839)	(0.614, 0.808)	(0.616, 0.798)	-	0.388	0.224	0.224	0.224

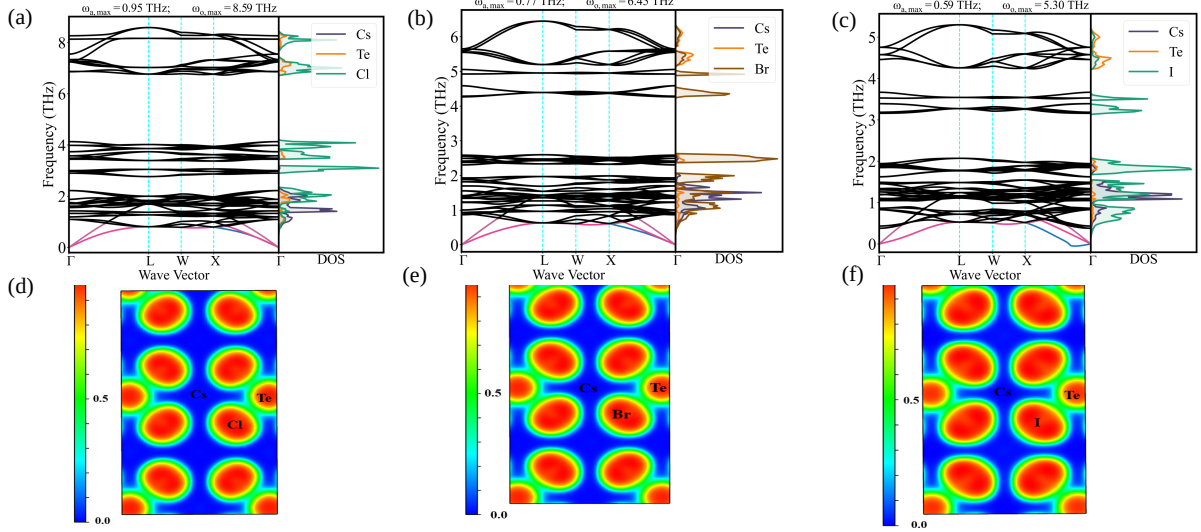


Figure 4: Phonon band structure along with DOS of (a)  $\text{Cs}_2\text{TeCl}_6$ , (b)  $\text{Cs}_2\text{TeBr}_6$ , and (c)  $\text{Cs}_2\text{TeI}_6$ . Electron localization function of (110) plane passing through constituent atoms in (d)  $\text{Cs}_2\text{TeCl}_6$ , (e)  $\text{Cs}_2\text{TeBr}_6$ , and (f)  $\text{Cs}_2\text{TeI}_6$ . The attached ELF scale of 0, 0.5, and 1.0 indicate electron depletion, delocalized and localized electron-like features, respectively.

#### 4.5 Mechanical properties

To address the mechanical properties of these systems such as stability of materials, hardness, ductility, brittleness, etc, we have computed the elastic moduli of these materials. The elastic moduli reveal the system's response to the applied stress along different directions [77]. As we have discussed in the section 4.1, these systems have FCC structures, hence these systems have only three independent elastic moduli  $C_{11}$ ,  $C_{12}$ , and  $C_{44}$ . The computed elastic constants are summarized in the following table 3. Here, the Cauchy pressure

Table 3: Mechanical properties of  $\text{Cs}_2\text{TeX}_6$  ( $X = \text{Cl}, \text{Br}, \text{I}$ ) vacancy ordered perovskites. All the elastic constants and moduli are expressed in GPa.

Parameters	$\text{Cs}_2\text{TeCl}_6$	$\text{Cs}_2\text{TeBr}_6$	$\text{Cs}_2\text{TeI}_6$
$C_{11}$ (GPa)	19.99	19.43	18.73
$C_{12}$ (GPa)	9.93	9.98	10.49
$C_{44}$ (GPa)	7.8	8.13	8.0
Shear Modulus G(GPa)	6.54	6.53	6.12
Bulk Modulus B(GPa)	13.29	13.13	13.23
Young Modulus Y (GPa)	16.86	16.82	15.91
Debye temperature $\Theta_D$ (K)	143.3	122	106.1
Longitudinal velocity $v_l$ (m/s)	2519.9	2231.65	2111.75
Transverse velocity $v_s$ (m/s)	1373.93	1220.83	1129.57
Average velocity $v_{av}$ (m/s)	1532.43	1361.32	1261.64

( $C_p = C_{12} - C_{44}$ ) is positive for all systems. However, it is higher for  $\text{Cs}_2\text{TeI}_6$  than for  $\text{Cs}_2\text{TeCl}_6$  and  $\text{Cs}_2\text{TeBr}_6$ , indicating that  $\text{Cs}_2\text{TeI}_6$  exhibits a greater degree of ionic character [78]. The shear modulus (G) quantifies a material's resistance to plastic deformation, whereas the bulk modulus (B) represents its ability to resist fracture. A  $B/G$  ratio  $\geq 1.75$  generally suggests a ductile nature, while a lower value indicates brittleness [79]. Our calculations reveal that all these systems exhibit a predominantly ductile nature. The sound velocities of  $\text{Cs}_2\text{TeX}_6$  ( $X=\text{Cl}, \text{Br}, \text{I}$ ) can be estimated from the computed elastic constants [80] and the calculated values

presented in the table 3. The sound velocities of these systems are comparable. In particular, the  $\text{Cs}_2\text{TeI}_6$  exhibits a lower sound velocity than  $\text{Cs}_2\text{TeBr}_6$  and  $\text{Cs}_2\text{TeCl}_6$ . This trend in sound velocity can be attributed to the higher atomic mass of the halogen atom. Since the Debye temperature is directly proportional to the average sound velocity, the lower sound velocity of  $\text{Cs}_2\text{TeI}_6$  results in a lower Debye temperature and becomes desirable for thermoelectric applications.

## 4.6 Transport properties

To assess the thermoelectric performance of these materials, we thoroughly examined their transport properties, such as electrical conductivity, thermal conductivity, Seebeck coefficient, power factor, and figure of merit. We made use of HSE06 calculated band gap along with PBE calculated electronic band structure including SOC to compute the transport properties. Our investigations predict  $\text{Cs}_2\text{TeI}_6$  as the best thermoelectric performer compared to other perovskites  $\text{Cs}_2\text{TeCl}_6$  and  $\text{Cs}_2\text{TeBr}_6$  under study. At the same time, the trends for transport properties show similar behavior as function of carrier concentration and temperature for these systems. Hence, here we discuss the factors responsible for the promising thermoelectric performance of  $\text{Cs}_2\text{TeI}_6$  in detail. The transport properties of  $\text{Cs}_2\text{TeCl}_6$  and  $\text{Cs}_2\text{TeBr}_6$  are given in supporting information.

### Electrical conductivity

The electrical conductivity ( $\sigma$ ) of  $\text{Cs}_2\text{TeI}_6$  for electron and hole doping as a function of carrier concentration over a temperature range of 300 K to 800 K is presented in Figures 5(a) and 6(a), respectively. The electrical conductivity is significantly higher for electron doping than for hole doping. This behavior is attributed to the presence of light carriers in highly dispersive conduction bands, in contrast to the heavy carriers present in flat valence bands, as shown in the table 2. At a low electron (hole) doping concentration of  $1 \times 10^{18} \text{ cm}^{-3}$  and at 300 K, the electrical conductivity is found to be  $9.93 \times 10^2 \text{ Sm}^{-1}$  ( $1.53 \times 10^2 \text{ Sm}^{-1}$ ). With increasing doping concentration, the electrical conductivity monotonically increases due to the semiconducting nature of these materials but decreases at high carrier concentrations due to an increased scattering rate. At a high electron (hole) doping concentration of  $1 \times 10^{21} \text{ cm}^{-3}$  and at 300 K,  $\sigma$  is found to be  $3.17 \times 10^5 \text{ Sm}^{-1}$  ( $7.50 \times 10^4 \text{ Sm}^{-1}$ ) for  $\text{Cs}_2\text{TeI}_6$ . With increase in temperature,  $\sigma$  reduces to be  $3 \times 10^2 \text{ Sm}^{-1}$  ( $2.89 \times 10^1 \text{ Sm}^{-1}$ ) at electron (hole) concentration of  $1 \times 10^{18} \text{ cm}^{-3}$  and at 800 K. This decrease in  $\sigma$  is caused by enhanced scattering at high temperatures. This decline in electrical conductivity is mainly attributed to decrease in carrier mobility at high temperatures and high carrier concentration. Figure 7(a) shows the carrier mobility as a function of carrier concentration for a range of temperature for  $\text{Cs}_2\text{TeI}_6$ . In the figure 7, the solid and dashed lines represent electron and hole doping, respectively. To delve deeper into the mobility limiting factors, we looked into the contributions of acoustic deformation potential (ADP), polar optical phonon (POP), and impurity (IMP) caused scattering, as depicted in figure 7 (b) at room temperature for electron and hole mobility. Our analysis reveals that IMP and POP mechanisms are the most dominant scattering processes in limiting mobility in comparison with the ADP scattering process. As shown in figure 7(b), when IMP and POP scattering contributions are smaller, total mobility is mainly limited by these mechanisms, as described by Matthiessen's rule [81]. Near room temperature, POP scattering is the dominant contributor, whereas IMP scattering becomes more significant at higher temperatures for both electrons and holes. Holes in  $\text{Cs}_2\text{TeI}_6$  exhibit significantly lower mobility than electrons, resulting in lower electrical conductivity for holes. Remarkably, the electrical conductivity of  $\text{Cs}_2\text{TeI}_6$  is comparable to state of the art thermoelectric materials, namely SnSe ( $1000 \text{ Sm}^{-1}$  at 323 K) [82], SnS ( $500 \text{ Sm}^{-1}$  at 323 K) [83], and Cu<sub>2</sub>Se ( $1500 \text{ Sm}^{-1}$  at 323 K) [84].

### Seebeck coefficient

To evaluate the potential difference produced by the thermal gradient, we evaluated the Seebeck coefficient (S) of  $\text{Cs}_2\text{TeI}_6$  as a function of carrier concentration for electron and hole doping, over a temperature range of 300 K to 800 K as shown in figures 5(b) and 6(b), respectively. As opposed to electrical conductivity, the Seebeck coefficient is consistently greater for hole doping as compared to electron doping across the considered

doping concentration range owing to high effective mass of holes as shown in the table 2. For instance, at an electron (hole) concentration of  $1 \times 10^{18} \text{ cm}^{-3}$  and 300 K, the Seebeck coefficient is found to be 440 (562)  $\mu\text{VK}^{-1}$  for  $\text{Cs}_2\text{TeI}_6$ . This difference is caused by the significantly heavier holes as compared to the electrons. This difference in magnitude of the Seebeck coefficient becomes more prominent with increase in temperature and 800 K, the Seebeck coefficient increases to be 577 (728)  $\mu\text{VK}^{-1}$ . The Seebeck coefficient values obtained for these materials are notably comparable to those reported for other double perovskites, such as  $\text{Rb}_2\text{AgBiX}_6$  ( $\text{X} = \text{Cl}, \text{Br}$ ) [85],  $\text{K}_2\text{AgAsX}_6$  ( $\text{X} = \text{halogen elements}$ ) [86], and  $\text{Cs}_2\text{BiAgX}_6$  ( $\text{X} = \text{halogen elements}$ ) [87],  $\text{K}_2\text{InBiX}_6$  ( $\text{X} = \text{Cl}, \text{Br}$ ) [88],  $\text{CH}_3\text{NH}_3\text{PbI}_3$  [89] as well as the commercially available  $\text{Bi}_2\text{Te}_3$  [90]. Increasing the doping concentration lowers the Seebeck coefficient further and at an electron (hole) concentration of  $1 \times 10^{18} \text{ cm}^{-3}$  and 300 K, it becomes 5 (74)  $\mu\text{VK}^{-1}$  and improves slightly with increase in temperature. These effects are in compliance with the Pisarenko relation [91]. These high values of the Seebeck coefficient for  $\text{Cs}_2\text{TeI}_6$  show this system's strong potential for thermoelectric applications.

### Electronic thermal conductivity

Figure 5(c) and 6(c) display the electronic thermal conductivity of  $\text{Cs}_2\text{TeI}_6$  as a function of carrier concentration over a temperature range of 300 K to 800 K for electron and hole doping, respectively. As  $\sigma$  and  $\kappa_e$  are proportional to each other by Wiedemann-Franz law,  $\kappa_e$  follows the similar trend like  $\sigma$  in this system  $\text{Cs}_2\text{TeI}_6$  for both electron and hole doping. Like  $\sigma$ , the  $\kappa_e$  increases with increase in carrier concentration and decreases with temperature as mobility decreases with increase in temperature (Figure 7). For instance, at an electron (hole) doping concentration of  $1 \times 10^{18} \text{ cm}^{-3}$  and 300 K,  $\kappa_e$  is calculated to be  $5.57 \times 10^{-3}$  ( $9.97 \times 10^{-4}$ )  $\text{Wm}^{-1}\text{K}^{-1}$ . These values are ultralow and favorable to design efficient thermoelectric devices. With increase in doping concentration, at  $1 \times 10^{21} \text{ cm}^{-3}$ ,  $\kappa_e$  enhances to be 2.02 (0.4)  $\text{Wm}^{-1}\text{K}^{-1}$ . Further with increase in temperature, it diminished to be 1.51 (0.2)  $\text{Wm}^{-1}\text{K}^{-1}$ . Such low values motivates us further to investigate the thermoelectric performance of this system  $\text{Cs}_2\text{TeI}_6$ .

### Thermoelectric power factor

With the above calculated transport properties, we evaluate the power factor ( $S^2\sigma$ ) in order to quantify its capability in power generation. Figure 5(d) and 6(d) show the thermoelectric power factor of  $\text{Cs}_2\text{TeI}_6$  as a function of carrier concentration for temperatures ranging from 300 K to 800 K for electron and hole doping, respectively. We reveal that the power factor initially increases with increase in carrier concentration, achieves maxima and then decreases with further increase in carrier concentration. This behavior stems from the trade-off behavior between the Seebeck coefficient and electrical conductivity. We find that the power factor is significantly higher for electron doping as compared to hole doping owing to increased electrical conductivity for electron doping. Our calculations reveal that the power factor maximizes to be 0.743 (0.535)  $\text{mWm}^{-1}\text{K}^{-2}$  at optimum electron (hole) carrier concentration of  $4.23 \times 10^{19}$  ( $3.10 \times 10^{20}$ )  $\text{cm}^{-3}$  and at 300 K. These values improve further with increase in temperature. For instance, the maximum power factor for electron doping is obtained to be 0.94 at electron concentration of  $1.21 \times 10^{20} \text{ cm}^{-3}$  at 800 K, whereas for hole doping, the maximum calculated power factor is 0.56  $\text{mWm}^{-1}\text{K}^{-2}$  at hole concentration of  $6.26 \times 10^{20} \text{ cm}^{-3}$  and at 500 K. These values are comparable to some state of the art thermoelectric materials, such as  $\text{PbTe}$ (2.5  $\text{mWm}^{-1}\text{K}^{-2}$ ) [92],  $\text{Bi}_2\text{Te}_3$  (n-type: 4.5  $\text{mWm}^{-1}\text{K}^{-2}$ , p-type: 3.0  $\text{mWm}^{-1}\text{K}^{-2}$ ) [93],  $\text{SnSe}$ (0.8  $\text{mWm}^{-1}\text{K}^{-2}$ ) [94],  $\text{Bi}_2\text{Se}_3$ (2.7  $\text{mWm}^{-1}\text{K}^{-2}$ ) [95],  $\text{Yb}_{14}\text{MnSb}_{11}$  (0.6  $\text{mWm}^{-1}\text{K}^{-2}$ ) [96],  $\text{CoSb}_3$ (1.6  $\text{mWm}^{-1}\text{K}^{-2}$ ) [97],  $\text{CsCdBr}_6$  (0.98  $\text{mWm}^{-1}\text{K}^{-2}$ ) [98],  $\text{CsCdCl}_6$  (0.41  $\text{mWm}^{-1}\text{K}^{-2}$ ) [98], and  $\text{K}_2\text{OsBr}_6$  (0.06  $\text{mWm}^{-1}\text{K}^{-2}$ ) [99].

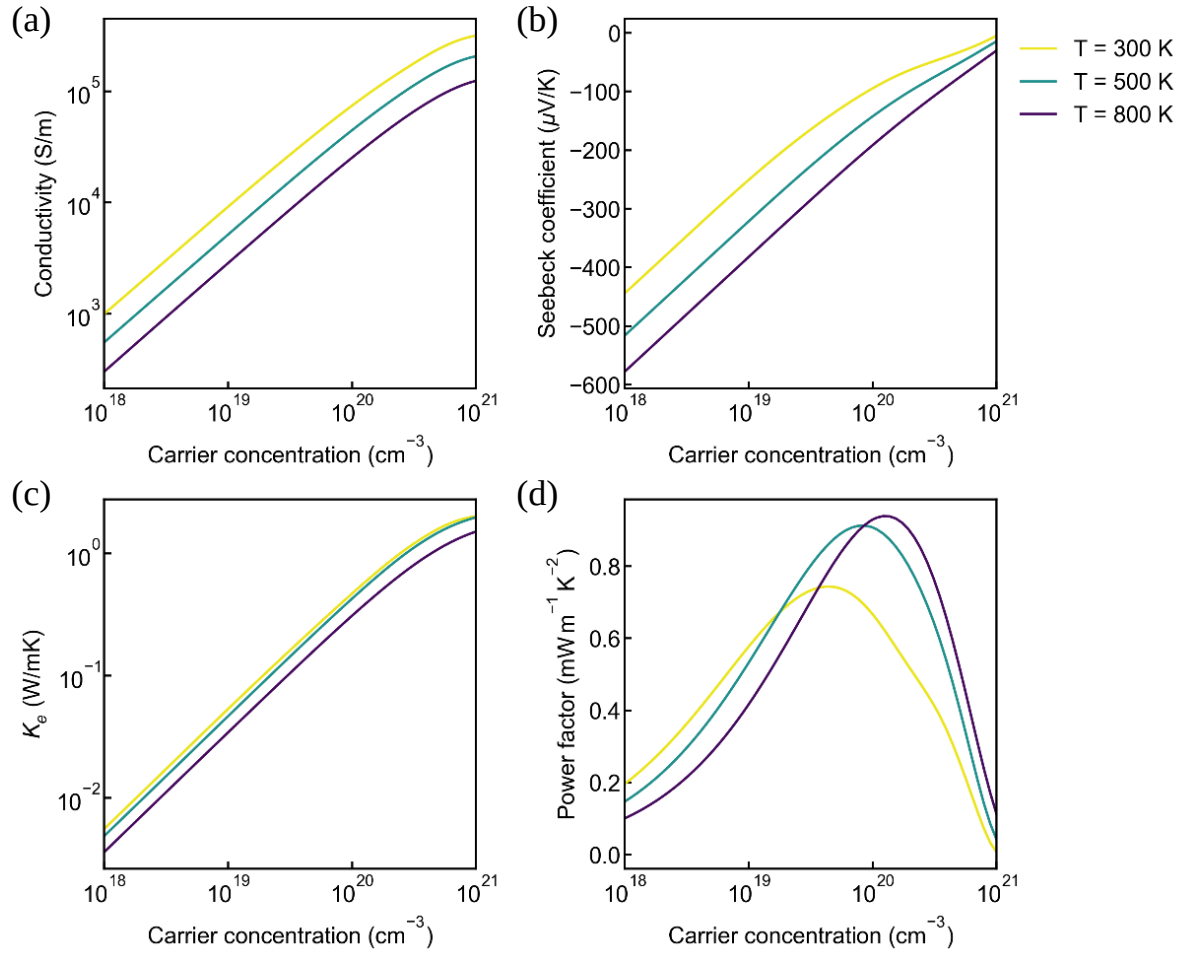


Figure 5: Transport properties of  $\text{Cs}_2\text{TeI}_6$  (a) electrical conductivity (b) Seebeck coefficient (c) electronic thermal conductivity (d) thermoelectric power factor for electron doping.

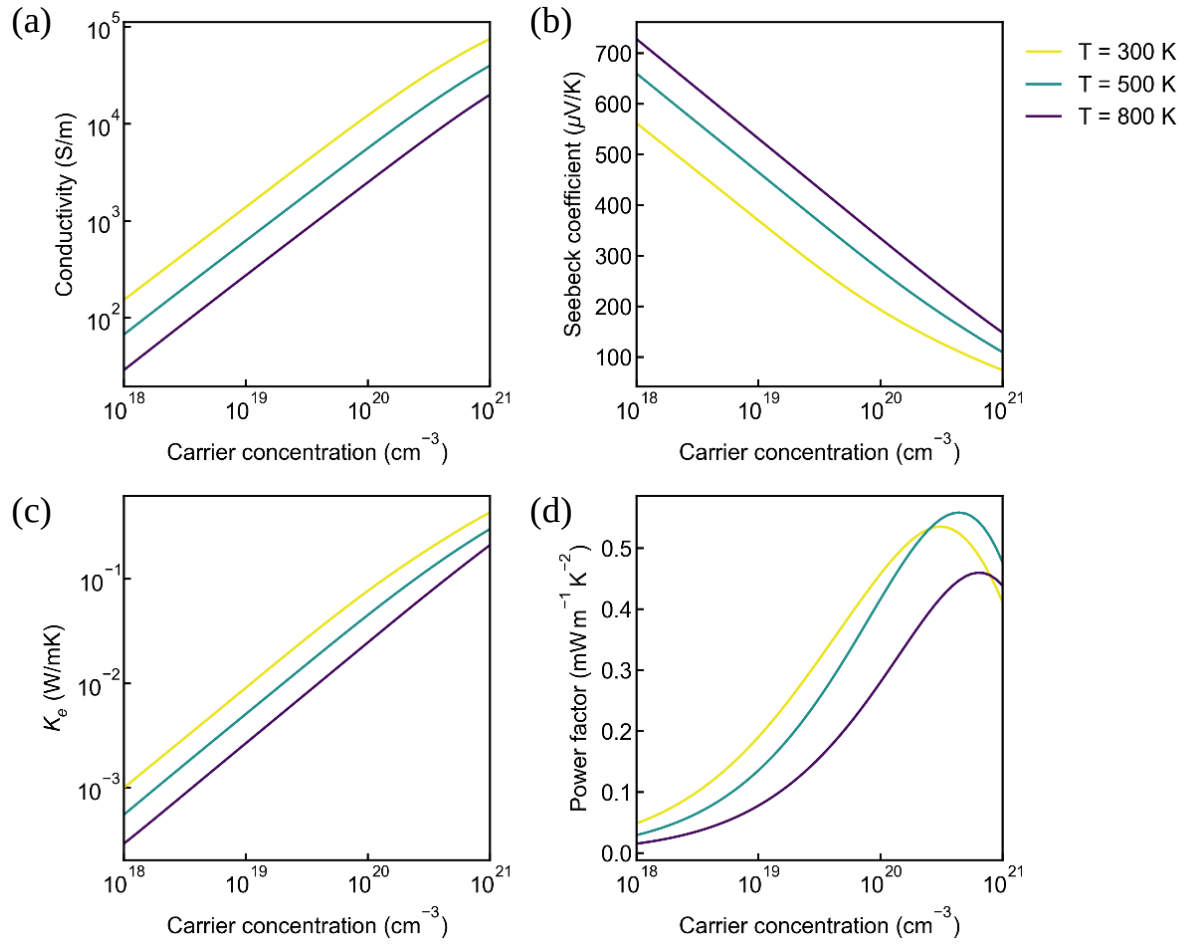


Figure 6: Transport properties of  $\text{Cs}_2\text{TeI}_6$  (a) electrical conductivity (b) Seebeck coefficient (c) electronic thermal conductivity (d) thermoelectric power factor for hole doping.

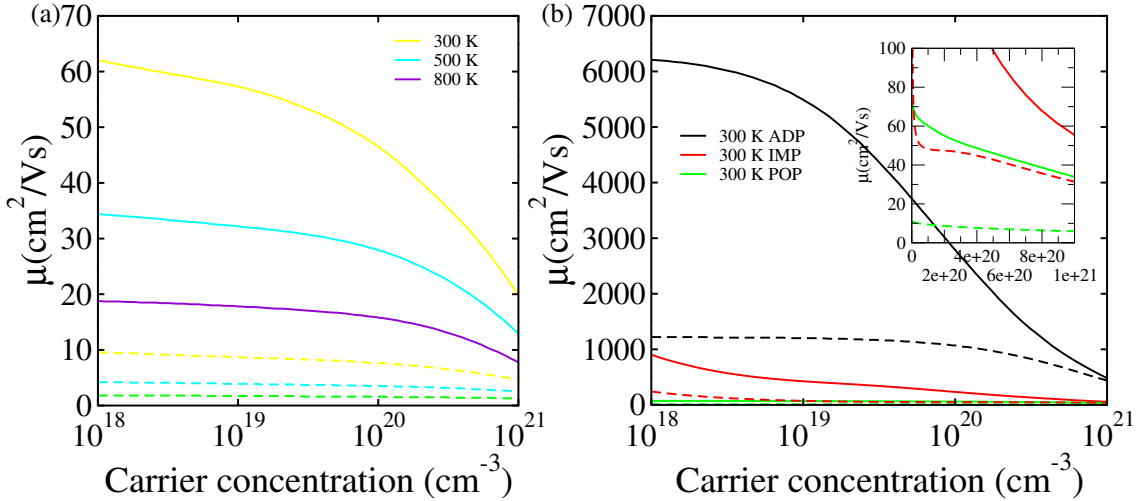


Figure 7: (a) electron and hole mobility of  $\text{Cs}_2\text{TeI}_6$ , (b) contribution of different scattering processes in overall mobility of  $\text{Cs}_2\text{TeI}_6$  for a range of temperature from 300 K to 800 K. The solid and dotted lines indicate electron and hole doping, respectively.

### Lattice thermal conductivity

Figure 8(a) displays the lattice thermal conductivity ( $\kappa_l$ ) as a function of temperature for  $\text{Cs}_2\text{TeI}_6$ .  $\kappa_l$  decreases as temperature increases following the temperature dependence as  $T^{-1}$  [100] as shown in the figure S1. This type of temperature variance with  $\kappa_l$  implies the dominance of Umklapp scattering in this system.  $\kappa_l$  was found to be  $0.41 \text{ Wm}^{-1}\text{K}^{-1}$  at room temperature. Such low values at room temperature are beneficial for better thermoelectric performance. The calculated  $\kappa_l$  is much lower than some well known thermoelectric materials namely,  $\text{Bi}_2\text{Te}_3 (1.24 \text{ Wm}^{-1}\text{K}^{-1})$  [101],  $\text{SnSe} (1.19 \text{ Wm}^{-1}\text{K}^{-1})$  [102],  $\text{Y}_2\text{Te}_3 (2.96 \text{ Wm}^{-1}\text{K}^{-1})$  [103], and  $\text{PbTe} (2.00 \text{ Wm}^{-1}\text{K}^{-1})$  [104]. Such perovskite materials are well known for low lattice thermal conductivity owing to their complex structure and weak bonds. In general, the lattice thermal conductivity of a solid depends upon three parameters namely, specific heat ( $C_v$ ), group velocity ( $v_g$ ), and relaxation time ( $\tau$ ) as given in the equation 1. The  $v_g$  and  $\tau$  parameters are the main deciding factors behind  $\kappa_l$  since  $C_v$  remains constant at room temperature and above. The macroscopic group velocity in  $\text{Cs}_2\text{TeI}_6$  is significantly low as given in table 3. Additionally, the low bulk modulus of these system suggest weaker bonds as given in the table 3 and weak bonds are more anharmonic and cause low lattice thermal conductivity [71]. This is also in compliance with our projected crystal orbital Hamilton population as discussed in section: 4.2. In addition to this, figure 8 (b) compares the average Grüneisen parameter of  $\text{Cs}_2\text{TeI}_6$  with other known thermoelectric materials. A larger Grüneisen parameter of  $\text{Cs}_2\text{TeI}_6$  indicates the lower lattice thermal conductivity [71]. Importantly, this value subsides further with increase in temperature and reaches to be  $0.18 \text{ Wm}^{-1}\text{K}^{-1}$  at 800 K. Scattering rate, especially phonon-phonon scattering becomes the dominating factor in lattice thermal conductivity at high temperatures as phonon population significantly enhances at high temperatures. There are three types of phonon-phonon scattering namely, normal scattering ( $\tau_N$ ), Umklapp scattering ( $\tau_{umk}$ ) and isotropic scattering ( $\tau_{iso}$ ). These scattering processes are caused by acoustic and optical phonons. In order to have a clear picture of these scattering mechanism, we plotted these relaxation time as function of temperature as given in the figure 8(c). Figure 8(c) displays the total relaxation time of acoustic and optical phonons. The total relaxation time is calculated using equation 2 as given in the Mattheissen's rule [81]. Though optical phonons scattering rate is significantly lower than acoustic phonons scattering, it does not directly affect the  $\kappa_l$  but offers resistance to acoustic phonons. This is also evident from the significant overlap of acoustic and optical modes in the figure 4. Notably, the relaxation time of acoustic phonons is lower too as compared to relaxation time in isotropic semiconductors. Further, we displayed the relaxation time of different acoustic modes in the figure 8(d). Figure 8(d) demonstrates that the relaxation

time associated with transverse acoustic (TA) mode is significantly lower than the longitudinal acoustic (LA) modes. In particular, the first transverse acoustic modes (TA1) significantly limits the  $\kappa_l$  of  $\text{Cs}_2\text{TeI}_6$ . We further analysed the inverse participation ratio (IPR) to figure out the real cause for such ultralow  $\kappa_l$  at the microscopic level. The IPR is defined in the equation 3, where  $N$  denotes the total number of atoms and  $u_{i\alpha q}$  indicates normalized eigenvector for  $i^{th}$  atom along  $\alpha$  direction and for  $q^{th}$  phonon mode. The IPR helps us to recognize the particular mode that contributes to ultralow  $\kappa_l$ . Figure 9 depicts the projected IPR vs frequency for the constituent atoms in the system  $\text{Cs}_2\text{TeI}_6$ . Our calculation reveals that Cs has highest contribution to IPR suggesting that the Cs atom is actively participating in scattering the phonons. Here we are neglecting the crucial contribution of Te to IPR at high frequency as these high frequency phonons do not play significant role in transport. The Cs dominated highest IPR is associated to particular modes around low frequencies  $34 \text{ cm}^{-1}$  and  $42 \text{ cm}^{-1}$ . The displacement pattern of these modes at  $\sim 34 \text{ cm}^{-1}$  and  $42 \text{ cm}^{-1}$  are displayed in figures 10(a) and (b), respectively. Figure 10(a) displays that the  $\text{TeI}_6$  octahedra shows tilting and asymmetric distortions along with neighbouring Cs atoms vibrating in opposite directions with different amplitudes. Such non-uniform and out-of-phase displacement modes break the periodicity required for phonon conduction, resulting into strong phonon scattering, thereby reduces the phonon mean free path and makes phonon less effective in carrying heat. Furthermore, figure 10 (b) represents the Cs atoms exhibiting large amplitude vertical displacement, while  $\text{TeI}_6$  octahedral network remains relatively rigid. Such displacement pattern confirms that Cs acts as a rattler ion inside a soft cage formed by  $\text{TeI}_6$  octahedral network. These low frequency Cs dominated vibrations strongly hinder the heat carrying acoustic phonons. Overall, the collective tilting of Te-I units and rattling like Cs vibrations turn the lattice network into phonon scattering network that strongly limits the phonon conduction. Here it is worth mentioning that these ultralow  $\kappa_l$  values are much desirable for efficient thermoelectric performance.

$$\kappa_l = \frac{1}{3} C_v v_g^2 \tau \quad (1)$$

$$\tau^{-1} = \tau_N^{-1} + \tau_{umk}^{-1} + \tau_{iso}^{-1} \quad (2)$$

$$\text{IPR} = \sum_{i=1}^N \left( \sum_{\alpha=1}^3 u_{i\alpha,q}^2 \right)^2 \quad (3)$$

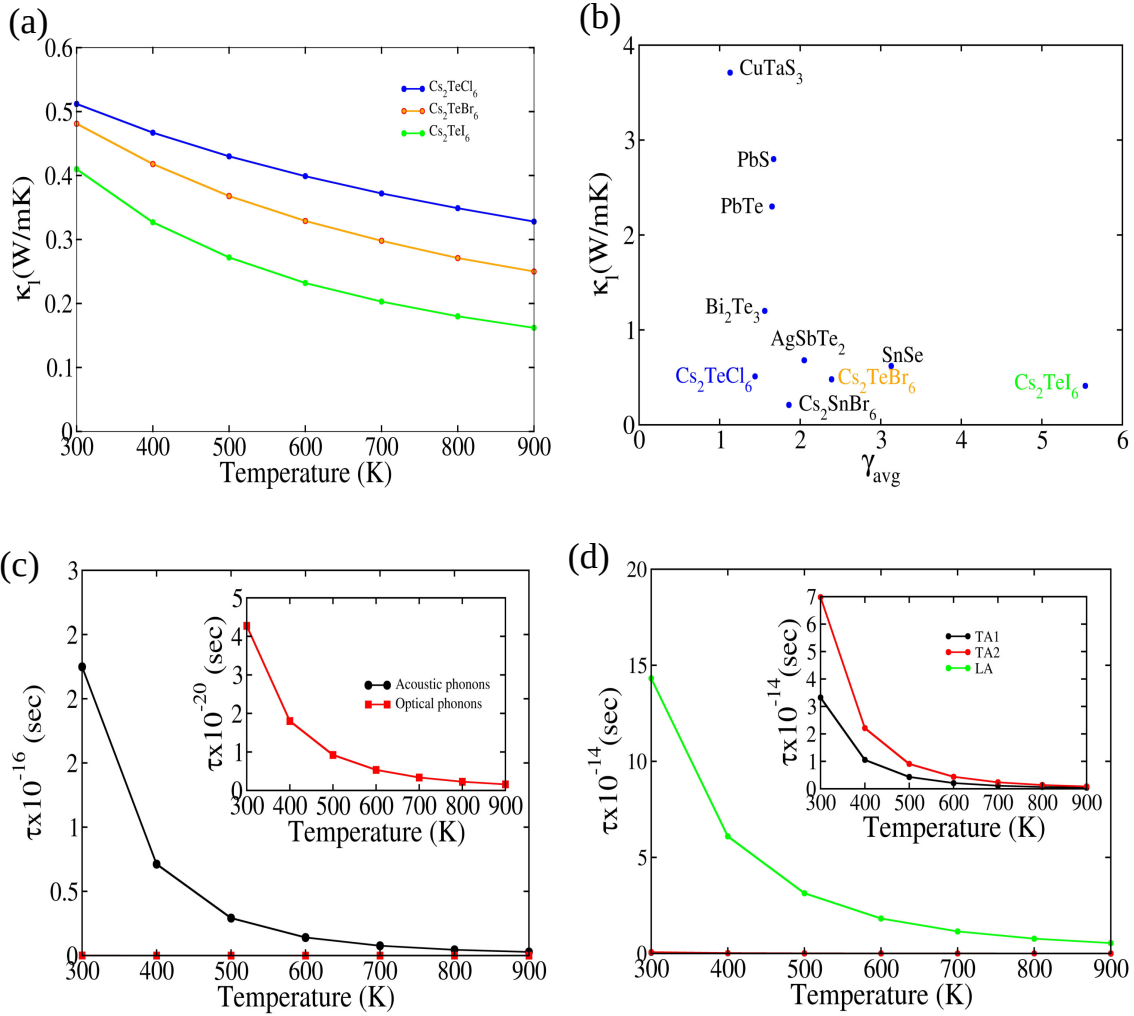


Figure 8: (a) Lattice thermal conductivity ( $\kappa_l$ ) as a function of the temperature of  $\text{Cs}_2\text{TeX}_6$  (X=Cl, Br, I), (b) Average Grüneisen parameter of known thermoelectric materials, (c) Relaxation time of acoustic and optical phonons, (d) Mode specific relaxation time of acoustic branch of  $\text{Cs}_2\text{TeI}_6$

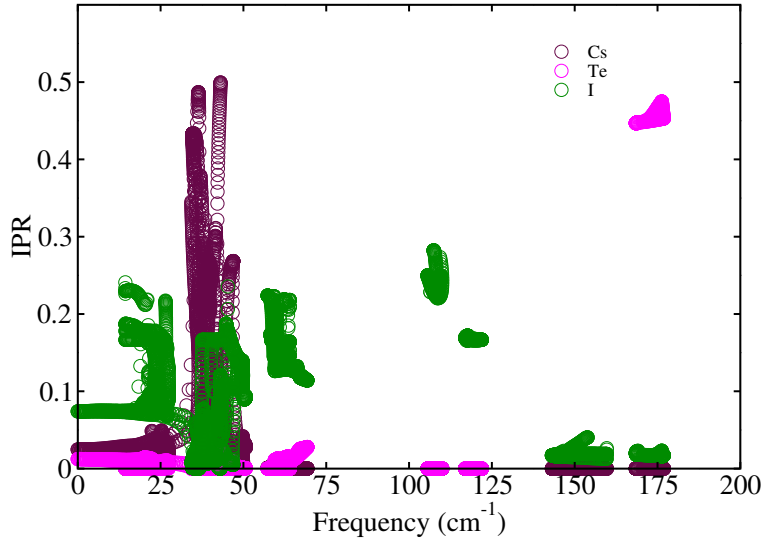


Figure 9: Inverse participation ratio as a function of frequency of  $\text{Cs}_2\text{TeI}_6$

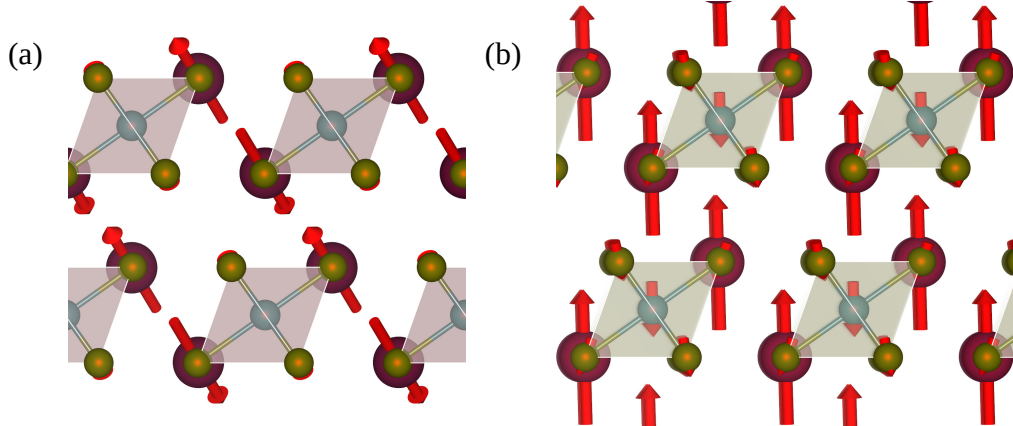


Figure 10: Displacement pattern associated to (a)  $34 \text{ cm}^{-1}$  and (b)  $42 \text{ cm}^{-1}$  for  $\text{Cs}_2\text{TeI}_6$

### Figure of Merit

Figure 11 illustrates the figure of merit as a function of carrier concentration and for a range of temperatures. Here, the solid lines and dashed lines indicate electron and hole doping, respectively. The highest ZT among  $\text{Cs}_2\text{TeX}_6$  ( $\text{X}=\text{Cl}, \text{Br}, \text{I}$ ) was found to be 1.97 at optimized carrier concentration  $3.35 \times 10^{19} \text{ cm}^{-3}$  and 800 K for n type doping in  $\text{Cs}_2\text{TeI}_6$ . However, for p-type doping in  $\text{Cs}_2\text{TeI}_6$ , the highest ZT was achieved to be 1.31 at hole concentration  $2.75 \times 10^{20} \text{ cm}^{-3}$  and 800 K. High Seebeck coefficient and electrical conductivity along with low thermal conductivity contributes to this elevated ZT in  $\text{Cs}_2\text{TeI}_6$  at such a low carrier concentration. Essentially, the suitable band curvature in the conduction band of  $\text{Cs}_2\text{TeI}_6$  along with the presence of octahedra in the local crystal structure are the reason behind such a high ZT. This ZT is higher than that of some state of the art thermoelectric materials namely,  $\text{Bi}_2\text{Te}_3$  ( 1.03 at 400 K) [105],  $\text{Bi}_2\text{Se}_3$  (1.14 at 300 K) [95],  $\text{CoSb}_3$ (0.43 at 600 K) [97],  $\text{SnTe}$  (1 at 900 K) [106],  $\text{PbTe}$  (1.96 at 700 K) [107],  $\text{SiGe}$  (1.84 at 1100 K) [108],  $\text{CsCdBr}_6$  (1.16 at 900 K) [98] and  $\text{Cs}_2\text{InAgCl}_6$  (0.74 at 700 K) [109]. Among the perovskite family, the ZT is significantly higher than that of many prospective modern latest thermoelectric materials, including,  $\text{CeMnO}_3$ (0.40) [110],  $\text{PrMnO}_3$  (0.47 at 500 K) [110],  $\text{CH}_3\text{NH}_3\text{PbI}_3$  (0.7) [111],  $\text{BiGaO}_3$

(0.62) [112],  $\text{SrTiO}_3$  (0.18) [113], and  $\text{Cs}_2\text{PdCl}/\text{Br}_6$  (0.71/0.76) [114].

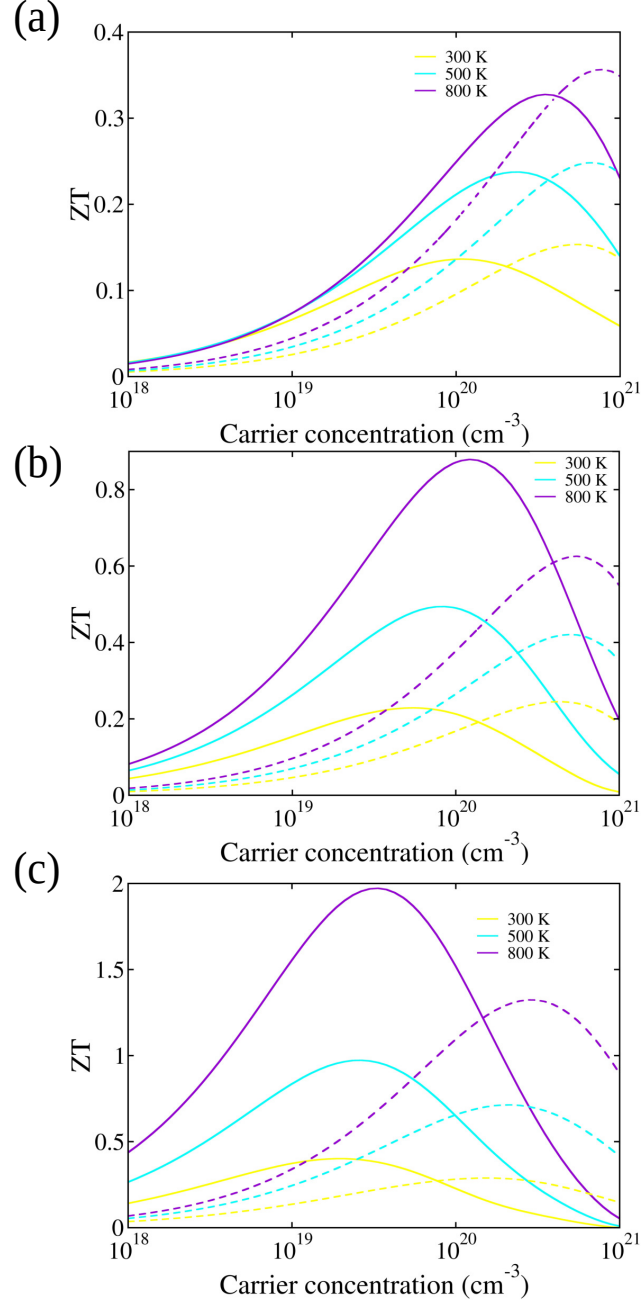


Figure 11: Figure of merit of (a)  $\text{Cs}_2\text{TeCl}_6$  (b)  $\text{Cs}_2\text{TeBr}_6$  (c)  $\text{Cs}_2\text{TeI}_6$  as a function of carrier concentration for 300 K, 500 K, and 800 K

## 5 Conclusions

To summarize, we carried out systematic calculations to predict the thermoelectric performance of  $\text{Cs}_2\text{TeX}_6$  ( $\text{X}=\text{Cl, Br, I}$ ) with both electron and hole doping. Our calculations reveal that these systems  $\text{Cs}_2\text{TeX}_6$

(X=Cl, Br, I) have cubic structure with electronic band gap of 3.27, 2.50, and 1.55 eV, respectively. These systems are mechanically and dynamically stable. We explored the effect of doping concentration upon the transport properties namely, Seebeck coefficient, electrical and thermal conductivity using the rigid band approach. We predict that  $\text{Cs}_2\text{TeI}_6$  has better thermoelectric performance than other systems in our study. With electron doping of  $3.35 \times 10^{19} \text{ cm}^{-3}$ , the figure of merit was found to be 1.97 at 800 K, whereas highest ZT is 1.31 for hole doping at hole concentration  $2.75 \times 10^{20} \text{ cm}^{-3}$  and at 800 K. This high ZT of this system stems from the suitable conduction band dispersion along with weak bonds in local structure that gives low macroscopic phonon velocity, in turn, ultralow lattice thermal conductivity. Such a high ZT at a low carrier concentration makes these materials unique in this area. Overall, the synergistic interplay between favorable band dispersion and ultralow lattice thermal conductivity renders  $\text{Cs}_2\text{TeI}_6$  as a strong candidate for high performance thermoelectric applications.

## 6 Acknowledgements

Authors gratefully acknowledge the computational resources provided by the Paramrudra High-Performance Computing (HPC) facility at the Inter-University Accelerator Centre (IUAC) New Delhi, C-DAC pune, IIT Jodhpur, and Sharda university Agra. The authors used ChatGPT to review the sentence structure and edited the content as required.

## 7 Declaration of competing interest

The authors claim no competing interest to report.

## References

- [1] Xiao Zhang and Li-Dong Zhao. Thermoelectric materials: Energy conversion between heat and electricity. *Journal of Materiomics*, 22, 04 2015.
- [2] Alessandro Simeone, Yang Luo, Elliot Woolley, Shahin Rahimifard, and Claudio Boér. A decision support system for waste heat recovery in manufacturing. *CIRP Annals*, 65(1):21–24, 2016.
- [3] Wolfgang G Zeier, Alex Zevalkink, Zachary M Gibbs, Geoffroy Hautier, Mercouri G Kanatzidis, and G Jeffrey Snyder. Thinking like a chemist: intuition in thermoelectric materials. *Angewandte Chemie International Edition*, 55(24):6826–6841, 2016.
- [4] Francis J DiSalvo. Thermoelectric cooling and power generation. *science*, 285(5428):703–706, 1999.
- [5] Ashish Kumar, Sahiba Bano, Bal Govind, A. Bhardwaj, Komal Bhatt, and D. K. Misra. A review on fundamentals, design and optimization to high zt of thermoelectric materials for application to thermoelectric technology. *Journal of Electronic Materials*, 50(11):6037–6059, Nov 2021.
- [6] Joseph R Sootsman, Duck Young Chung, and Mercouri G Kanatzidis. New and old concepts in thermoelectric materials. *Angewandte Chemie International Edition*, 48(46):8616–8639, 2009.
- [7] Woochul Kim. Strategies for engineering phonon transport in thermoelectrics. *J. Mater. Chem. C*, 3:10336–10348, 2015.
- [8] Shiqiang Hao, Vinayak P. Dravid, Mercouri G. Kanatzidis, and Christopher Wolverton. Computational strategies for design and discovery of nanostructured thermoelectrics. *npj Computational Materials*, 5(1):58, May 2019.
- [9] Bingchao Qin, Dongyang Wang, and Li-Dong Zhao. Slowing down the heat in thermoelectrics. *InfoMat*, 3(7):755–789, 2021.

[10] Hossein Asnaashari Eivari, Z Sohbatzadeh, P Mele, and MHN Assadi. Low thermal conductivity: fundamentals and theoretical aspects in thermoelectric applications. *Materials Today Energy*, 21:100744, 2021.

[11] A SI Bhalla, Ruyan Guo, and Rustum Roy. The perovskite structure—a review of its role in ceramic science and technology. *Materials research innovations*, 4(1):3–26, 2000.

[12] Guan Zhang, Gang Liu, Lianzhou Wang, and John TS Irvine. Inorganic perovskite photocatalysts for solar energy utilization. *Chemical Society Reviews*, 45(21):5951–5984, 2016.

[13] Hongchao Wang, Wenbin Su, Jian Liu, and Chunlei Wang. Recent development of n-type perovskite thermoelectrics. *Journal of Materomics*, 2(3):225–236, 2016.

[14] Md Azimul Haque, Seyoung Kee, Diego Rosas Villalva, Wee-Liat Ong, and Derya Baran. Halide perovskites: thermal transport and prospects for thermoelectricity. *Advanced Science*, 7(10):1903389, 2020.

[15] S Hébert, Delphine Flahaut, Christine Martin, S Lemonnier, J Noudem, C Goupil, A Maignan, and Jiri Hejtmanek. Thermoelectric properties of perovskites: Sign change of the seebeck coefficient and high temperature properties. *Progress in Solid State Chemistry*, 35(2-4):457–467, 2007.

[16] Tingjun Wu and Peng Gao. Development of perovskite-type materials for thermoelectric application. *Materials*, 11(6):999, 2018.

[17] Soonil Lee, Gaiying Yang, Rudeger HT Wilke, Susan Trolier-McKinstry, and Clive A Randall. Thermopower in highly reduced n-type ferroelectric and related perovskite oxides and the role of heterogeneous nonstoichiometry. *Physical Review B—Condensed Matter and Materials Physics*, 79(13):134110, 2009.

[18] Hao Wang, Chunqian Zhang, Wenqi Huang, Xiaoping Zou, Zhenyu Chen, Shengliu Sun, Lixin Zhang, Junming Li, Jin Cheng, Shixian Huang, et al. Research progress of abx 3-type lead-free perovskites for optoelectronic applications: materials and devices. *Physical Chemistry Chemical Physics*, 24(45):27585–27605, 2022.

[19] Farzaneh Arabpour Roghabadi, Maryam Alidaei, Seyedeh Maryam Mousavi, Tahereh Ashjari, Ali Shokrolahzadeh Tehrani, Vahid Ahmadi, and Seyed Mojtaba Sadrameli. Stability progress of perovskite solar cells dependent on the crystalline structure: From 3d abx 3 to 2d ruddlesden–popper perovskite absorbers. *Journal of Materials Chemistry A*, 7(11):5898–5933, 2019.

[20] Huanhuan Yao, Faguang Zhou, Zhizai Li, Zhipeng Ci, Liming Ding, and Zhiwen Jin. Strategies for improving the stability of tin-based perovskite (asn<sub>x</sub>3) solar cells. *Advanced Science*, 7(10):1903540, 2020.

[21] Longbin Qiu, Sisi He, Luis K Ono, and Yabing Qi. Progress of surface science studies on abx3-based metal halide perovskite solar cells. *Advanced Energy Materials*, 10(13):1902726, 2020.

[22] Md Helal Miah, Mayeen Uddin Khandaker, Md Bulu Rahman, Mohammad Nur-E-Alam, and Mohammad Aminul Islam. Band gap tuning of perovskite solar cells for enhancing the efficiency and stability: issues and prospects. *RSC advances*, 14(23):15876–15906, 2024.

[23] Edson Meyer, Dorcas Mutukwa, Nyengerai Zingwe, and Raymond Taziwa. Lead-free halide double perovskites: a review of the structural, optical, and stability properties as well as their viability to replace lead halide perovskites. *Metals*, 8(9):667, 2018.

[24] Fatemeh Heidari Gourji and Dhayalan Velauthapillai. A review on cs-based pb-free double halide perovskites: From theoretical and experimental studies to doping and applications. *Molecules*, 26(7):2010, 2021.

[25] Ye Wu, Xiaoming Li, and Haibo Zeng. Lead-free halide double perovskites: structure, luminescence, and applications. *Small Structures*, 2(3):2000071, 2021.

[26] Liang Chu, Waqar Ahmad, Wei Liu, Jian Yang, Rui Zhang, Yan Sun, Jianping Yang, and Xing'ao Li. Lead-free halide double perovskite materials: a new superstar toward green and stable optoelectronic applications. *Nano-Micro Letters*, 11:1–18, 2019.

[27] Loreta A Muscarella and Eline M Hutter. Halide double-perovskite semiconductors beyond photovoltaics. *ACS Energy Letters*, 7(6):2128–2135, 2022.

[28] Femi Igbari, Zhao-Kui Wang, and Liang-Sheng Liao. Progress of lead-free halide double perovskites. *Advanced Energy Materials*, 9(12):1803150, 2019.

[29] Lei Lu, Xiong Pan, Junhua Luo, and Zhihua Sun. Recent advances and optoelectronic applications of lead-free halide double perovskites. *Chemistry—A European Journal*, 26(71):16975–16984, 2020.

[30] Sukanya Ghosh, Hari Shankar, and Prasenjit Kar. Recent developments of lead-free halide double perovskites: a new superstar in the optoelectronic field. *Materials Advances*, 3(9):3742–3765, 2022.

[31] Tao Zuo, Fangfang Qi, ChiYung Yam, and Lingyi Meng. Lead-free all-inorganic halide double perovskite materials for optoelectronic applications: progress, performance and design. *Physical Chemistry Chemical Physics*, 24(44):26948–26961, 2022.

[32] Md Azimul Haque, Seyoung Kee, Diego Rosas Villalva, Wee-Liat Ong, and Derya Baran. Halide perovskites: thermal transport and prospects for thermoelectricity. *Advanced Science*, 7(10):1903389, 2020.

[33] Ye Wu, Xiaoming Li, and Haibo Zeng. Lead-free halide double perovskites: structure, luminescence, and applications. *Small Structures*, 2(3):2000071, 2021.

[34] Qianqian Fan, Gill V Biesold-McGee, Jianzhong Ma, Qunna Xu, Shuang Pan, Juan Peng, and Zhiqun Lin. Lead-free halide perovskite nanocrystals: crystal structures, synthesis, stabilities, and optical properties. *Angewandte Chemie International Edition*, 59(3):1030–1046, 2020.

[35] Sayed Ali Khan, Noor Zamin Khan, Muhammad Sohail, Marcin Runowski, Xin Xu, and Simeon Agathopoulos. Recent developments of lead-free halide-perovskite nanocrystals: Synthesis strategies, stability, challenges, and potential in optoelectronic applications. *Materials Today Physics*, 34:101079, 2023.

[36] Qianqian Fan, Gill V Biesold-McGee, Jianzhong Ma, Qunna Xu, Shuang Pan, Juan Peng, and Zhiqun Lin. Lead-free halide perovskite nanocrystals: crystal structures, synthesis, stabilities, and optical properties. *Angewandte Chemie International Edition*, 59(3):1030–1046, 2020.

[37] Lei Lei, Qi Dong, Kenan Gundogdu, and Franky So. Metal halide perovskites for laser applications. *Advanced Functional Materials*, 31(16):2010144, 2021.

[38] Haiyun Dong, Chunhuan Zhang, Xiaolong Liu, Jiannian Yao, and Yong Sheng Zhao. Materials chemistry and engineering in metal halide perovskite lasers. *Chemical Society Reviews*, 49(3):951–982, 2020.

[39] Fei Yan, Swee Tiam Tan, Xiao Li, and Hilmi Volkan Demir. Light generation in lead halide perovskite nanocrystals: Leds, color converters, lasers, and other applications. *Small*, 15(47):1902079, 2019.

[40] Fuxiang Ji, Gerrit Boschloo, Feng Wang, and Feng Gao. Challenges and progress in lead-free halide double perovskite solar cells. *Solar RRL*, 7(6):2201112, 2023.

[41] Zewen Xiao and Yanfa Yan. Progress in theoretical study of metal halide perovskite solar cell materials. *Advanced Energy Materials*, 7(22):1701136, 2017.

[42] Woochul Lee, Huashan Li, Andrew B Wong, Dandan Zhang, Minliang Lai, Yi Yu, Qiao Kong, Elbert Lin, Jeffrey J Urban, Jeffrey C Grossman, et al. Ultralow thermal conductivity in all-inorganic halide perovskites. *Proceedings of the National Academy of Sciences*, 114(33):8693–8697, 2017.

[43] Nawzad A Abdulkareem, Sarkawt A Sami, and Badal H Elias. Structural, electronic and optical properties of cubic perovskite  $\text{cspbx}_3$  ( $x = \text{br, cl}$  and  $\text{i}$ ). *Science Journal of University of Zakho*, 8(1):23–28, 2020.

[44] Warda Rahim, Anjie Cheng, Chenyang Lyu, Tianyi Shi, Ziheng Wang, David O Scanlon, and Robert G Palgrave. Geometric analysis and formability of the cubic  $\text{a}_2\text{bx}_6$  vacancy-ordered double perovskite structure. *Chemistry of Materials*, 32(22):9573–9583, 2020.

[45] Muhammad Faizan, Xinjiang Wang, Shaimaa AM Abdelmohsen, KC Bhamu, Subrahmanyam Sappati, Amel Laref, Nisar Muhammad, Muhammad Mushtaq, Ashraf MM Abdelbacki, and Rabah Khenata. Understanding the electronic structure and optical properties of vacancy-ordered double perovskite  $\text{a}_2\text{bx}_6$  for optoelectronic applications. *Energy & Fuels*, 36(13):7065–7074, 2022.

[46] Muhammad Faizan, Guoqi Zhao, Tianxu Zhang, Xiaoyu Wang, Xin He, and Lijun Zhang. Elastic and thermoelectric properties of vacancy ordered double perovskites  $\text{a}_2\text{bx}_6$ : a dft study. *Acta Physico-Chimica Sinica*, 40(1):2303004, 2024.

[47] Muhammad Faizan, Guoqi Zhao, Tianxu Zhang, Xiaoyu Wang, Xin He, and Lijun Zhang. Elastic and thermoelectric properties of vacancy ordered double perovskites  $\text{a}_2\text{bx}_6$ : a dft study. *Acta Physico-Chimica Sinica*, 40(1):2303004, 2024.

[48] Animesh Bhui, Tanmoy Ghosh, Koushik Pal, Kewal Singh Rana, Kaushik Kundu, Ajay Soni, and Kanishka Biswas. Intrinsically low thermal conductivity in the n-type vacancy-ordered double perovskite  $\text{cs}_2\text{sni}_6$ : octahedral rotation and anharmonic rattling. *Chemistry of Materials*, 34(7):3301–3310, 2022.

[49] Preeti Bhumla, Manjari Jain, Sajjan Sheoran, and Saswata Bhattacharya. Vacancy-ordered double perovskites  $\text{cs}_2\text{bi}_6$  ( $b = \text{pt, pd, te, sn}$ ): an emerging class of thermoelectric materials. *The Journal of Physical Chemistry Letters*, 13(50):11655–11662, 2022.

[50] Isabel Vazquez-Fernandez, Silvia Mariotti, Oliver S Hutter, Max Birkett, Tim D Veal, Theodore DC Hobson, Laurie J Phillips, Lefteris Danos, Pabitra K Nayak, Henry J Snaith, et al. Vacancy-ordered double perovskite  $\text{cs}_2\text{tei}_6$  thin films for optoelectronics. *Chemistry of Materials*, 32(15):6676–6684, 2020.

[51] Jun Guo, Yadong Xu, Wenhui Yang, Bao Xiao, Qihao Sun, Xinlei Zhang, Binbin Zhang, Menghua Zhu, and Wanqi Jie. High-stability flexible x-ray detectors based on lead-free halide perovskite  $\text{cs}_2\text{tei}_6$  films. *ACS Applied Materials & Interfaces*, 13(20):23928–23935, 2021.

[52] Jinye Li, Chengjun Lei, Pengjie Jiang, Chen Xu, Tingting Liu, and Xiao Liang. An energy-efficient tellurium electrode enabled by a  $\text{cs}_2\text{tei}_6$  perovskite structure for durable aqueous  $\text{zn-te}$  batteries. *Energy & Environmental Science*, 17(22):8633–8642, 2024.

[53] Qiang Huang, Jiang Zhu, Fei Qi, Li Zhang, Feifan Chen, Yayun Pu, Nan Zhang, Manjing Wang, Weiwei Chen, and Xiaosheng Tang. Ultraviolet–visible photodetector based on a  $\text{cs}_2\text{tei}_6$  thin film. *ACS Applied Electronic Materials*, 2025.

[54] Byunghong Lee, Constantinos C. Stoumpos, Nanjia Zhou, Feng Hao, Christos Malliakas, Chen-Yu Yeh, Tobin J. Marks, Mercouri G. Kanatzidis, and Robert P. H. Chang. Air-stable molecular semiconducting iodosalts for solar cell applications:  $\text{Cs}_2\text{sni}_6$  as a hole conductor. *Journal of the American Chemical Society*, 136(43):15379–15385, 2014. PMID: 25299304.

[55] Yadong Xu, Bo Jiao, Tze-Bin Song, Constantinos C Stoumpos, Yihui He, Ido Hadar, Wenwen Lin, Wanqi Jie, and Mercouri G Kanatzidis. Zero-dimensional cs<sub>2</sub>tei<sub>6</sub> perovskite: solution-processed thick films with high x-ray sensitivity. *Acs Photonics*, 6(1):196–203, 2018.

[56] Annalise E Maughan, Alex M Ganose, Mitchell M Bordelon, Elisa M Miller, David O Scanlon, and James R Neilson. Defect tolerance to intolerance in the vacancy-ordered double perovskite semiconductors cs<sub>2</sub>sni<sub>6</sub> and cs<sub>2</sub>tei<sub>6</sub>. *Journal of the American Chemical Society*, 138(27):8453–8464, 2016.

[57] A Bekhti Siad, M Baira, and MB Siad. Structural, mechanical, optoelectronic and thermoelectric properties of double perovskite compounds cs<sub>2</sub>tex<sub>6</sub> (x= br, i) for energy storage applications: first principles investigations. *Journal of Physics and chemistry of solids*, 152:109955, 2021.

[58] Jing-Jing Zheng, Chao-jun Li, Rong-Rong Ma, Bao-Tian Wang, and Jiang-Jiang Ma. Bonding hierarchy and phonon coherence enhanced ultralow lattice thermal conductivity and excellent thermoelectric properties in cs<sub>2</sub>tei<sub>6</sub>. *Chinese Physics Letters*, 2025.

[59] G. Kresse and J. Furthmüller. Efficient iterative schemes for ab initio total-energy calculations using a plane-wave basis set. *Phys. Rev. B*, 54:11169–11186, Oct 1996.

[60] G. Kresse and J. Furthmüller. Efficiency of ab-initio total energy calculations for metals and semiconductors using a plane-wave basis set. *Computational Materials Science*, 6(1):15–50, 1996.

[61] P. E. Blöchl. Projector augmented-wave method. *Phys. Rev. B*, 50:17953–17979, Dec 1994.

[62] In-Ho Lee and Richard M Martin. Applications of the generalized-gradient approximation to atoms, clusters, and solids. *Physical Review B*, 56(12):7197, 1997.

[63] Jochen Heyd, Gustavo E Scuseria, and Matthias Ernzerhof. Hybrid functionals based on a screened coulomb potential. *The Journal of chemical physics*, 118(18):8207–8215, 2003.

[64] Ryky Nelson, Christina Ertural, Janine George, Volker L Deringer, Geoffroy Hautier, and Richard Dronskowski. Lobster: Local orbital projections, atomic charges, and chemical-bonding analysis from projector-augmented-wave-based density-functional theory. *Journal of computational chemistry*, 41(21):1931–1940, 2020.

[65] Atsushi Togo, Laurent Chaput, Terumasa Tadano, and Isao Tanaka. Implementation strategies in phonopy and phono3py. *Journal of Physics: Condensed Matter*, 35(35):353001, jun 2023.

[66] Alex M. Ganose, Junsoo Park, Alireza Faghaninia, Rachel Woods-Robinson, Kristin A. Persson, and Anubhav Jain. Efficient calculation of carrier scattering rates from first principles. *Nature Communications*, 12(1):2222, Apr 2021.

[67] Alex M. Ganose, Adam J. Jackson, and David O. Scanlon. sumo: Command-line tools for plotting and analysis of periodic \*ab initio\* calculations. *Journal of Open Source Software*, 3(28):717, 2018.

[68] Koichi Momma and Fujio Izumi. Vesta: A three-dimensional visualization system for electronic and structural analysis. *Journal of Applied Crystallography - J APPL CRYST*, 41:653–658, 06 2008.

[69] Tao Fan and Artem R. Oganov. Aicon: A program for calculating thermal conductivity quickly and accurately. *Computer Physics Communications*, 251:107074, 2020.

[70] Vasyl Sidey, O. ZUBAKA, and I. STERCHO. X-ray rietveld structure refinement and bond-valence analysis of cs<sub>2</sub>tei<sub>6</sub>. *Chemistry of Metals and Alloys*, 3:108–114, 01 2010.

[71] Ching Hua Lee and Chee Kwan Gan. Anharmonic interatomic force constants and thermal conductivity from grüneisen parameters: An application to graphene. *Physical Review B*, 96(3):035105, 2017.

[72] Md Sajib Hossain, Majibul Babu, Alamgir Kabir, Ahmed Azzouz Rached, and Ibrahim Kholil. A dft insight into lead free double halide perovskite  $cs_2tei_6$  for clean and renewable energy sources. *Materials Advances*, 2025.

[73] Maria C. Folgueras, Jianbo Jin, Mengyu Gao, Li Na Quan, Julian A. Steele, Shivani Srivastava, Michael B. Ross, Rui Zhang, Fabian Seeler, Kerstin Schierle-Arndt, Mark Asta, and Peidong Yang. Lattice dynamics and optoelectronic properties of vacancy-ordered double perovskite  $cs_2tex_6$  ( $x = cl-, br-, i-$ ) single crystals. *The Journal of Physical Chemistry C*, 125(45):25126–25139, 2021.

[74] M.E. El Goutni, H. Aboura, T. Benmessabih, M. Batouche, T. Seddik, O.Y. Khyzhun, and Tuan V. Vu. The effect of heavy and light electronic bands on thermoelectric properties of  $mg_2si_1-xsnx$  alloys: Insights from an ab-initio study. *Chemical Physics*, 564:111729, 2023.

[75] Lydia Rathnam, Surabhi Suresh Nair, Arnab Ganguly, Nirpendra Singh, and Gobind Das. Strategies to enhance thermoelectric performance: Review. *Journal of Materials Research and Technology*, 37:2694–2717, 2025.

[76] Jan-Hendrik Pöhls, Zhe Luo, Umut Aydemir, Jon-Paul Sun, Shiqiang Hao, Jiangang He, Ian Hill, Geoffroy Hautier, Anubhav Jain, Xiaoqin Zeng, Chris Wolverton, Jeff Snyder, Hong Zhu, and Mary White. First-principles calculations and experimental studies of:  $Xyz$  2 thermoelectric compounds: Detailed analysis of van der waals interactions. *Journal of Materials Chemistry A*, 6, 10 2018.

[77] S Qiu, Bjorn Clausen, SA Padula II, RD Noebe, and R Vaidyanathan. On elastic moduli and elastic anisotropy in polycrystalline martensitic niti. *Acta Materialia*, 59(13):5055–5066, 2011.

[78] D. G. Pettifor. Theoretical predictions of structure and related properties of intermetallics. *Materials Science and Technology*, 8(4):345–349, 1992.

[79] S.F. Pugh. Xcii. relations between the elastic moduli and the plastic properties of polycrystalline pure metals. *The London, Edinburgh, and Dublin Philosophical Magazine and Journal of Science*, 45(367):823–843, 1954.

[80] Kanchana Venkatakrishnan, Ganapathy Vaitheeswaran, P. Souvatzis, O Eriksson, and S Lebègue. Density functional study of the electronic structure and lattice dynamics of  $srcl_2$ . *Journal of physics. Condensed matter : an Institute of Physics journal*, 22:445402, 11 2010.

[81] Yann-Michel Niquet, Viet-Hung Nguyen, François Trionzon, Ivan Duchemin, Olivier Nier, and Denis Rideau. Quantum calculations of the carrier mobility: Methodology, matthiessen's rule, and comparison with semi-classical approaches. *Journal of Applied Physics*, 115(5), 2014.

[82] Wei Wei, Cheng Chang, Teng Yang, Jizi Liu, Huaichao Tang, Jian Zhang, Yusheng Li, Feng Xu, Zhidong Zhang, Jing-Feng Li, et al. Achieving high thermoelectric figure of merit in polycrystalline  $snse$  via introducing  $sn$  vacancies. *Journal of the American Chemical Society*, 140(1):499–505, 2018.

[83] Binqiang Zhou, Shuai Li, Wen Li, Juan Li, Xinyue Zhang, Siqi Lin, Zhiwei Chen, and Yanzhong Pei. Thermoelectric properties of  $sns$  with  $na$ -doping. *ACS applied materials & interfaces*, 9(39):34033–34041, 2017.

[84] Ying He, Tristan Day, Tiansong Zhang, Huili Liu, Xun Shi, Lidong Chen, and G Jeffrey Snyder. High thermoelectric performance in non-toxic earth-abundant copper sulfide. *Advanced Materials*, 26(23):3974–3978, 2014.

[85] A. Mebed, Samah Al-Qaisi, and Malak Azmat Ali. Study of optoelectronic and thermoelectric properties of double perovskites  $rb_2agbx_6$  ( $x = br, i$ ): by dft approach. *The European Physical Journal Plus*, 137, 08 2022.

[86] Malak Azmat Ali, Razan Alshgari, Aboud Bahajjaj, and Mika Sillanpää. The study of new double perovskites  $k_2ag_2as_x$ 6 ( $x=cl, br$ ) for energy-based applications. *Journal of Taibah University for Science*, 17:2170680, 02 2023.

[87] Enamul Haque and M. Hossain. Origin of ultra-low lattice thermal conductivity in  $cs_2bi_2ag_x$ 6 ( $x=cl, br$ ) and its impact on thermoelectric performance. *Journal of Alloys and Compounds*, 748, 03 2018.

[88] Debidatta Behera and Sanat Kumar Mukherjee. Theoretical investigation of the lead-free  $k_2in_2bx_6$  ( $x=cl, br$ ) double perovskite compounds using ab initio calculation. *JETP Letters*, 116(8):537–546, 2022.

[89] Akash Shukla, Vipan Kumar Sharma, Saral Kumar Gupta, and Ajay Singh Verma. Investigations of fundamental physical and thermoelectric properties of methylammonium lead iodide ( $ch_3nh_3pb_i3$ ) perovskites. *Materials Research Express*, 6(12):126323, 2020.

[90] Gang Zhou and Dong Wang. Few-quintuple  $bi_2te_3$  nanofilms as potential thermoelectric materials. *Scientific Reports*, 5(1):8099, Jan 2015.

[91] Chong Xiao, Zhou Li, Kun Li, Pengcheng Huang, and Yi Xie. Decoupling interrelated parameters for designing high performance thermoelectric materials. *Accounts of chemical research*, 47, 02 2014.

[92] Hongchao Wang, Junphil Hwang, Matthew Loren Snedaker, Il-ho Kim, Chanyoung Kang, Jungwon Kim, Galen D Stucky, John Bowers, and Woochul Kim. High thermoelectric performance of a heterogeneous pbte nanocomposite. *Chemistry of Materials*, 27(3):944–949, 2015.

[93] LM Goncalves, C Couto, P Alpuim, AG Rolo, Friedemann Völklein, and JH Correia. Optimization of thermoelectric properties on  $bi_2te_3$  thin films deposited by thermal co-evaporation. *Thin Solid Films*, 518(10):2816–2821, 2010.

[94] Li-Dong Zhao, Shih-Han Lo, Yongsheng Zhang, Hui Sun, Gangjian Tan, Ctirad Uher, Christopher Wolverton, Vinayak P Dravid, and Mercouri G Kanatzidis. Ultralow thermal conductivity and high thermoelectric figure of merit in snse crystals. *nature*, 508(7496):373–377, 2014.

[95] Muhammad Zamir Mohyedin, Mohamad Fariz Mohamad Taib, Afiq Radzwan, M Mustaffa, Amiruddin Shaari, Oskar Hasdinor Hassan, Ab Malik Marwan Ali, Bakhtiar Ul Haq, and Muhd Zu Azhan Yahya. Enhanced mechanism of thermoelectric performance of  $bi_2se_3$  using density functional theory. *Materials for Renewable and Sustainable Energy*, 9(3):15, 2020.

[96] Shawna R Brown, Susan M Kauzlarich, Franck Gascoin, and G Jeffrey Snyder.  $Yb_{14}mnsb_{11}$ : New high efficiency thermoelectric material for power generation. *Chemistry of materials*, 18(7):1873–1877, 2006.

[97] Julia Santana-Andreo, Antonio M Márquez, Jose J Plata, Ernesto J Blancas, José-Luis González-Sánchez, Javier Fdez Sanz, and Pinku Nath. High-throughput prediction of the thermal and electronic transport properties of large physical and chemical spaces accelerated by machine learning: Charting the  $zt$  of binary skutterudites. *ACS Applied Materials & Interfaces*, 16(4):4606–4617, 2024.

[98] Wenqiu Shang, Tao Hu, Ding Li, Shichang Li, Xianju Zhou, Chunbao Feng, and Dengfeng Li. Combined first-principles and machine learning study of thermal transport and thermoelectric properties of p-type halide perovskite  $cscdx_3$  ( $x= cl, br$ ). *Journal of Electronic Materials*, pages 1–10, 2024.

[99] Rehan Ullah, Malak Azmat Ali, G Murtaza, Afzal Khan, and Asif Mahmood. Ab initio study for the structural, electronic, magnetic, optical, and thermoelectric properties of  $k_2osx_6$  ( $x= cl, br$ ) compounds. *International Journal of Energy Research*, 44(11):9035–9049, 2020.

[100] Micheline Roufosse and PG Klemens. Thermal conductivity of complex dielectric crystals. *Physical Review B*, 7(12):5379, 1973.

[101] Olle Hellman and David A Broido. Phonon thermal transport in  $\text{Bi}_2\text{Te}_3$  from first principles. *Physical Review B*, 90(13):134309, 2014.

[102] Li-Dong Zhao, Shih-Han Lo, Yongsheng Zhang, Hui Sun, Gangjian Tan, Ctirad Uher, Christopher Wolverton, Vinayak P Dravid, and Mercouri G Kanatzidis. Ultralow thermal conductivity and high thermoelectric figure of merit in  $\text{SnSe}$  crystals. *nature*, 508(7496):373–377, 2014.

[103] Michael Y Toriyama, Dean Cheikh, Sabah K Bux, G Jeffrey Snyder, and Prashun Gorai.  $\text{Y}_2\text{Te}_3$ : A new n-type thermoelectric material. *ACS Applied Materials & Interfaces*, 14(38):43517–43526, 2022.

[104] Zhiting Tian, Jivtesh Garg, Keivan Esfarjami, Takuma Shiga, Junichiro Shiomi, and Gang Chen. Phonon conduction in  $\text{PbSe}$ ,  $\text{PbTe}$ , and  $\text{PbTe}_{1-x}\text{Se}_x$  from first-principles calculations. *Physical Review B—Condensed Matter and Materials Physics*, 85(18):184303, 2012.

[105] Fengrong Yu, Bo Xu, Jianjun Zhang, Dongli Yu, Julong He, Zhongyuan Liu, and Yongjun Tian. Structural and thermoelectric characterizations of high pressure sintered nanocrystalline  $\text{Bi}_2\text{Te}_3$  bulks. *Materials Research Bulletin*, 47(6):1432–1437, 2012.

[106] Gangjian Tan, Li-Dong Zhao, Fengyuan Shi, Jeff W Doak, Shih-Han Lo, Hui Sun, Chris Wolverton, Vinayak P Dravid, Ctirad Uher, and Mercouri G Kanatzidis. High thermoelectric performance of p-type  $\text{SnTe}$  via a synergistic band engineering and nanostructuring approach. *Journal of the American Chemical Society*, 136(19):7006–7017, 2014.

[107] Abhiyan Pandit and Bothina Hamad. Thermoelectric and lattice dynamics properties of layered  $\text{mx}$  ( $\text{m}=\text{Sn, Pb}$ ;  $\text{x}=\text{s, Te}$ ) compounds. *Applied surface science*, 538:147911, 2021.

[108] EMRE Güler, MELEK Güler, Şule Uğur, and Gökay Uğur. First principles investigations of the electronic, elastic, mechanical, anisotropic, optical, and thermoelectric performance of monoclinic  $\text{SiGe}$  semiconductors. *International Journal of Modern Physics B*, 38(26):2450355, 2024.

[109] Enamul Haque and M Anwar Hossain. High seebeck coefficient and ultra-low lattice thermal conductivity in  $\text{Cs}_2\text{InAgCl}_6$ . *arXiv preprint arXiv:1802.08136*, 2018.

[110] Shakeel Ahmad Khandy and Dinesh C Gupta. Investigation of the transport, structural and mechanical properties of half-metallic  $\text{FeMn}_3$  ( $\text{re}=\text{Ce}$  and  $\text{Pr}$ ) ferromagnets. *RSC advances*, 6(100):97641–97649, 2016.

[111] Akash Shukla, Vipan Kumar Sharma, Saral Kumar Gupta, and Ajay Singh Verma. Investigations of fundamental physical and thermoelectric properties of methylammonium lead iodide ( $\text{CH}_3\text{NH}_3\text{PbI}_3$ ) perovskites. *Materials Research Express*, 6(12):126323, 2020.

[112] Rasul Bakhsh Behram, MA Iqbal, SM Alay-e Abbas, M Sajjad, M Yaseen, M Imran Arshad, and G Murtaza. Theoretical investigation of mechanical, optoelectronic and thermoelectric properties of  $\text{BiGaO}_3$  and  $\text{BiInO}_3$  compounds. *Materials Science in Semiconductor Processing*, 41:297–303, 2016.

[113] Akeem Adekunle Adewale, Abdullah Chik, Ruhiyuddin Mohd Zaki, Faizul Che Pa, Yeoh Cheow Keat, and Noorina Hidayu Jamil. Dft study of thermoelectric performance of  $\text{SrTiO}_3$  doped by tantalum. *International Journal of Nanoelectronics & Materials*, 12(4), 2019.

[114] KC Bhamu, Amit Soni, and Jagrati Sahariya. Revealing optoelectronic and transport properties of potential perovskites  $\text{Cs}_2\text{PbX}_6$  ( $\text{x}=\text{Cl, Br}$ ): a probe from density functional theory (dft). *Solar Energy*, 162:336–343, 2018.